ELECTRICAL AND TOPOLOGICAL CHARACTERIZATION OF THIN FILM TRANSISTORS BASED ON A NOVEL ORGANIC SEMICONDUCTOR FOR BIOSENSING APPLICATIONS

by

SALAHEDDIN SOMMAKIA

A Thesis submitted to the

Graduate School-New Brunswick

Rutgers, The State University of New Jersey

and

The Graduate School of Biomedical Sciences

University of Medicine and Dentistry of New Jersey

in partial fulfillment of the requirements

for the degree of

Master of Science

Graduate Program in Biomedical Engineering

written under the direction of

Prof. Yves J. Chabal

and approved by

New Brunswick, New Jersey

October, 2007

ABSTRACT OF THE THESIS

ELECTRICAL AND TOPOLOGICAL CHARACTERIZATION OF THIN FILM TRANSISTORS BASED ON A NOVEL ORGANIC SEMICONDUCTOR FOR BIOSENSING APPLICATIONS

By: SALAHEDDIN SOMMAKIA

Thesis Director: Prof. Yves J. Chabal

The design of sensors capable of detecting various analytes has important biosensing applications ranging from medical diagnostics to air quality monitoring. Organic-based semiconductors are being promoted as biosensors for their cost-effectiveness, facility of fabrication and potential for reaction to many analytes. This study aims to characterize the electrical performance and topology of thin film transistors (TFTs) based on a novel semiconducting molecule with a conjugated phenyl-thiophene core, 5-5'-bis-4-(6-hydroxyhexyloxy)-phenyl-2-2'-bithiophene (or HOC6PTTPC6OH for short). Electrical measurements show that working TFTs can be fabricated from this novel material and exhibit consistent transistor performance. Atomic Force Microscopy reveals a polycrystalline structure with distinct grains separated by crevices, the degree of which depends on the deposition process. The electrical performance (measured by the field effect mobility) is shown to depend on the topology, and therefore on the details of film deposition. Based on these findings, possible improvements to the fabrication method to optimize electrical performance and sensing response are discussed with relation to future studies on these devices as alcohol vapor sensors, and potentially, as DNA sensors.

ACKNOWLEDGEMENTS

This thesis documents my research, which is but a small part of a bigger ongoing project that I had the privilege and pleasure of being part of. This research could not have been completed was it for not the patience and graciousness of numerous people who took time away from their busy schedules to listen to me and offer advice and insightful comments. I would especially like to thank the following people, without whose valuable input this thesis could not have come into being:

Prof. Yves Chabal for giving me the chance to be part of his research group and for his continuous advice and mentorship;

Dr. Adrian Mann and Dr. Jeffrey Zahn for serving on my committee and offering numerous important tips and pointers;

Melissa Stokes for patiently training me, closely working with me, continuously providing feedback and graciously helping me rehearse my defense ;

Dr. Jean-François Veyan for his valuable assistance with the hardware modifications;

Norman Lapin for helpful discussions and moral support;

Dr. Lezsek Wielunski for assisting with the Rutherford Back Scattering experiments;

Dr. Kin P. Cheung and Yun Wang for granting me access to their equipment and providing helpful comments;

Prof. Michael Gershenson for allowing me access to the AFM and Dr. David Olaya for training me to use it;

DEDICATION

To my family whose love and faith in me has propelled me to where I am now, and my friends whose devotion and support made the journey through graduate school so enjoyable.

Contents

List of Tables

List of Figures

Chapter 1

Introduction

1.1 Motivation

The design of sensors capable of detecting various analytes has important implications in a wide variety of applications, from medical diagnostics to air quality monitoring. These sensors can be realized through various sensing elements including, but not limited to, quartz crystal microbalance (QCM) [1, 2], Metal oxide [3, 4] and conducting polymer [5, 6] chemiresistors.

In addition to the previously mentioned sensing elements, many studies have been performed on the use of organic semiconductors as biosensors [7, 8, 9, 10, 11]. Katz et al. [12] have shown that one organic semiconductor, 6PTTP (very close in structure to our examined molecule) can sense DMMP, *a nerve gas simulant*. This has huge defense and security implications, and provides additional incentive for more organic semiconductor biosensor research. One of the main advantages of using organic semiconductors as biosensors is cost. This is especially important for biosensors, because many of their applications, such as glucose and DNA sensors and breathalyzers, mandate temporary usage and disposability. Organic semiconductors have the advantage of being much cheaper to produce than their inorganic counterparts for several rea-

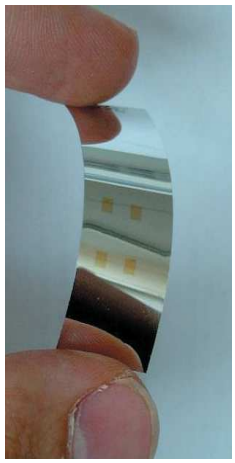

Figure 1.1: Organic thin film transistors fabricated on a flexible substrate (Taken from [13])

sons. Unlike silicon and other inorganic semiconductors which require high energy and contaminant free clean rooms, organic semiconductors are synthesized by wet chemistry techniques and can be made to be solution processable [14]. This facilitates inexpensive fabrication methods like spin-coating [15] and inkjet printing [16], and can be deposited onto plastic [16], for instance, and mylar [13], which allows for flexible devices (such as the devices shown in Figure 1.1). Organic semiconductors are already gaining hold in applications like optoelectronics [17] and active-matrix display driving circuits [18] and the most recent research shows that the mobilities of organic semiconductor molecules can rival those of amorphous silicon [19].

Of course, there are some disadvantages to organic semiconductors, including low charge carrier mobilities and on/off current ratios which prevent their use in high speed switching circuit, and durability issues in that they are prone to atmospheric degeneration. These drawbacks can be somewhat overlooked in biosensing applications, since they do not require extremely fast devices and by definition do not require a long life span for the devices, but rather temporary or even one time use.

The goal of this project is to closely examine the properties of thin film transistors fabricated with a novel organic semiconductor molecule, 5-5′-bis-4-(6-hydroxyhexyloxy)-

phenyl-2-2′-bithiophene (HOC6PTTPC6OH), with an eye for immediate applications in alcohol vapor sensing, and potential future applications in DNA sensing (with the determination of a stable crosslinker). Electrical properties of the film, as indicated by the field effect mobility, were studied for different fabrication parameters using a probe station setup coupled with a precision semiconductor parameter analyzer, and topological characteristics of the deposited films were examined using atomic force microscopy to elucidate the relationship between the fabrication parameters, electrical performance and nanoscale topological properties of the film.

1.2 Background

1.2.1 Organic semiconductors

Energy bands and conduction states

Depending on the material, charge carriers can be ions, electrons or holes (regions of space from which the negative has been removed). As atoms are brought together, their energy levels split into a ground level and excited level. The simplest example is that of two hydrogen atoms, whose wave functions are given as ψ_A and ψ_B. When they are brought close together, the wave function for the new system will be given as [20]:

$$\psi = \psi_A^1 \psi_B^2 \pm \psi_A^2 \psi_B^1 \tag{1.1}$$

with $\psi_A^1 \psi_B^2 + \psi_A^2 \psi_B^1$ corresponding to the lower energy level, and $\psi_A^1 \psi_B^2 - \psi_A^2 \psi_B^1$ to the higher energy level. Now, in a solid, the presence of large number of molecules in a very limited space fixed in a definite lattice causes the spacing between the energy levels to become negligible, and the energy levels converge into energy bands. The bands are called the *conduction* and *valence* band.

In conductors, free electrons are abundant and carry enough energy to be in the conduction band, or the conduction band overlaps the valence band. In insulators, the valence band is full, the conduction band is empty and there is a large energy gap between the two bands. Semiconductors represent a center ground between the two, where there is a reduced width of the energy gap, which enables the behavior of semiconductors to switch between the conduction and insulation. The term *doping* is employed to describe when electrons gain enough energy to cross the band gap. Doping is intrinsic if the energy is supplied thermally (i.e. through interaction with lattice vibrations —phonons—), through absorption of radiation, or by an electric field. It is extrinsic if it is induced by lattice imperfections or impurities. The latter method is the most prevalent in inorganic semiconductors, where introduction of electron donating impurity atoms gives rise to n-type semiconductors, while electron accepting impurity atoms result in p-type semiconductors.

Charge conduction in organic semiconductors

Organic compounds are usually thought of as insulators. However, it was noticed that some organic materials, namely, conjugated organic molecules, are capable of conducting electric current and can display semiconductor behavior. To better understand this phenomenon it is important to note that electrons are categorized by bonding energy, and the following list shows some the categories as related to single and double bond formation [21]:

1. core electrons: localized to specific nuclei.

2. σ-electrons: localized between bonded nuclei.

3. n-electrons: associated with heteroatoms, and are more important for reactivity than for bonding.

4. π-electrons: involved in bonding. π bonds are weaker and less localized than

σ-bonds, and are orthogonal to σ-bonds. π-electrons move in the field set up by the disposition of core, n and σ-electrons. They are less tightly bound to their respective nuclei than σ-electrons.

Conjugated organic molecules, which have an alternation of single and double bonds (of which π bonds are an important component), have a "cloud" of π-electrons delocalized over the whole molecule [22] that can gain energy with intrinsic doping and move from the valence to the conduction band, and thus films made from the conjugated organic molecule can act as semiconductor devices.

In organic semiconductors, the terms p-type and n-type have a different meaning than in their inorganic counterpart. They do not imply the presence of certain impurity atoms, but rather the type of majority carriers. For p-type organic semiconductors, the majority carriers are holes, while for n-type, the majority carriers are electrons. Most organic semiconductors to fate are p-type [23].

The order of the organic semiconductor molecules within the film is critical for achieving good charge transport. When the film is amorphous, there many gaps within the film that act as electron traps. The conduction occurs through "hopping" between localized states. Mobility can be improved by altering the film morphology by moving from amorphous to polycrystalline to single crystal. Another method is too add attach strong electron withdrawing groups to increase the molecule's electron affinity, Ea [23].

1.2.2 Organic Thin Film Transistors

Field effect transistors function by modulating the current passing through a conducting channel between a source and a drain electrode by applying a variable voltage to a third electrode, called the gate. The organic field effect transistors under study in this thesis are p-type thin film transistors (TFTs). This means that the channel is made of a p-type organic semiconductor, and a layer of dielectric insulates the gate

from the channel, forming a capacitor.

If no voltage is applied to the gate, the free carriers (holes) are homogeneously distributed within the channel. The conductance of the channel is very small due to the low density of the carriers, and the current between the source and drain electrodes is very low. If a negative potential is applied to the gate, an excess of holes will be attracted to the semiconductor-dielectric interface and concentrate in a very thin layer. This increased density will allow a significant conductance to arise in the channel. For a positive gate potential, depending on the material, a depletion of charge carriers can occur in the semiconductor channel, and if the positive potential is sufficiently high, this depletion region could span the whole thickness of the channel.

Field Effect Mobility

The field effect mobility of a TFT quantifies average charge carrier drift velocity per unit area [24]. Calculation methods will be discussed in depth in section 3.1.3. It is used as a measure of the performance of TFTs; almost all studies that discuss improving device performance attempt doing so by increasing the calculated mobility for the devices in question. The most common approach for increasing the mobility for a deposited film is to ensure the grains growing on the substrate are large and continuous with as few grain boundaries as possible [25, 26, 27]. This has been shown to be achievable by employing slow deposition rates [28, 29] and by heating the substrate during deposition [30, 26, 31].

Example values of field effect mobility reported in the literature for various materials are shown in table 1.1. It should be noted that these mobilities for devices not fabricated under the same conditions as in this thesis. Some devices were fabricated on substrates other than SiO_2, with gates other than doped Si, with various substrate coatings, or with heated substrates. Also, the mobility calculations in some cases were calculated differently to incorporate a multitude of trapping and other

Table 1.1: Mobility values for some organic semiconductors

Organic Semiconductor	Mobility ($cm^2V^{-1}s^{-1}$)	Date	Source
Pentacene	0.8; 1.5	2003	[28],[32]
α-6T	0.01	2004	[33]
α-8T	0.2	2000	[34]
rubrene (single crystal)	15.4	2004	[35]
variety of phenylene-thiophene compounds	10^{-5}–0.09	2003	[36]
6PTTP	0.01	2004	[37]

mobility-lowering effects, thus significantly increasing the calculated mobility.

1.2.3 Organic Thin Film Transistors as Gas Sensors

The basic concept of a gas sensor is an organic TFT running in saturation, and when this TFT is exposed to the gas of interest the saturation current will drop. The gas in question might be water vapor in nitrogen [10] or hexanol in air or a multitude of potential analytes that can be sensed with a wide variety of organic semiconductors [9]. Although the exact mechanism by which these gaseous analytes cause a drop in the conductance of the channel is still unknown, it is generally accepted that the topology of the film plays an important role. Since most organic semiconductors exhibit rough polycrystalline grains with multiple crevices between the grains, the gas molecules can intercalate between these crevices, where they interact with the film. The exact mechanism is not known, and it is hoped that follow up experiments to this thesis involving *in situ* IR spectroscopy of such films during exposure to gaseous analytes will elucidate this point.

1.2.4 Choice of material

Studies have been performed on oligoacenes, oligothiophenes, and conjugated molecules with phenyl-thiophene cores to which HOC6PTTPC6OH belongs as mentioned above.

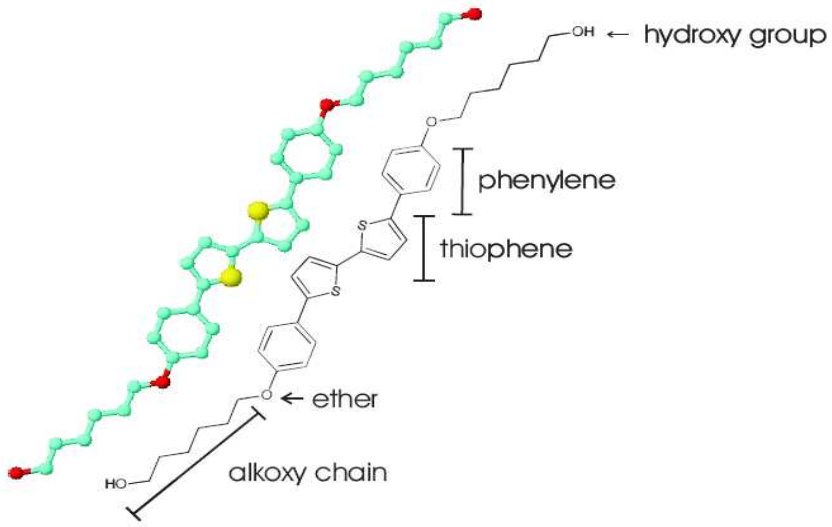

Figure 1.2: Molecular Structure of HOC6PTTPC6OH, from [38]

To the best of author's knowledge, HOC6PTTPC6OH has not been tested in organic TFTs before. Its molecular structure is shown in Figure **1.2.4**, taken from [38]. It was chosen for its conjugated phenylene-thiophene core, a component of other molecules that have displayed semiconductor performance [36, 37]. The hydroxyl termination adds a charge to the end of the alkyl chain, potentially offering a link site for biomolecules [39]. A study by Katz et al. [40] has shown that the addition of alkyl chains to α-6T results in a 25 fold increase in mobility; thus the rationale for choosing a molecule with an alkyl chain. Additionally, it is hypothesized that the alkyl chain will allow for spacing between the molecules, providing intercalation sites for biological anlaytes.

Chapter 2

Device Fabrication

2.1 Sample Preparation

In this study, we use wafers of heavily doped silicon ($\rho = 0.007\ \Omega m$) on which 1100Å of SiO_2 (as determined with Rutherford Back Scattering) were thermally deposited. From these wafers, we cut chips with an approximate area of 1 square inch using a diamond tipped cutter. These chips are hereafter referred to as "samples".

2.1.1 Solvent Cleaning

New, unused samples are cleaned with a combination of deionized water, acetone and isopropanol. The sample is placed in a beaker and submerged with the deionized water, then acetone is added gradually as the water is removed. The sample is allowed is allowed to sit in the acetone for a sufficient time and "swished" occasionally to allow for good cleaning. Acetone leaves a residue on the silicon samples if allowed to dry on them. Therefore, enough acetone is left to keep the sample submerged, and isopropanol is then used to displace the acetone in the same way that acetone displaced the deionized water.

After the acetone has been displaced completely by the isopropanol, the remaining

isopropanol is poured out and the sample is dried under a stream of dry nitrogen and is ready for the deposition process.

2.1.2 Piranha Cleaning

Previously used samples are cleaned with piranha. Piranha solution is a one step cleaning procedure employed primarily to remove organic residues from silicon samples. The solution consists of a 3:1 mixture of sulphuric acid (H_2SO_4, 100%) and hydrogen peroxide (H_2O_2, 30%). Piranha is a strong etchant of organic residues, and therefore it was used in these experiments to clean silicon samples on which films of organic material had been previously deposited in order to reuse them, provided that no damage has occurred to the samples through excessive scratching or oxide breakdowns. Piranha hyroxylates the silicon oxide layer, resulting in a thin hydroxyl terminated SiO_2 layer.

The solution is prepared under a fume hood using extreme caution, as the mixture reaction is exothermic and generates a lot of heat [41]. The peroxide is added to the acid, and the solution is given a sufficient amount of time to stabilize. The sample to be cleaned is slowly immersed in the piranha solution, and the beaker is placed on a hot plate to maintain the temperature at 90C°for at least 10 minutes. The heat is then turned off, the solution iteratively diluted with deionized water (approximately 1 liter) and the sample rinsed then dried under a stream of dry nitrogen.

This process was used sparingly, since it was uncertain that the gold contacts were removed completely from previously used devices. A hazy pattern corresponding to the shape of the gold contacts was observed in some of the samples, even after rigorous piranha cleaning.

2.2 Fabrication of the devices using thermal vacuum deposition

The device fabrication entails preparing the samples for the vacuum deposition, achieving a good vacuum within the evaporator chamber, thermal deposition of the appropriate material through resistive heating, accurate measurement of the thickness of the deposited film and the rate of deposition using a Quartz Crystal Microbalance (QCM), and post-deposition processing of the devices in preparation for the electrical measurements.

2.2.1 Pre-Deposition

For samples on which transistor devices are to be fabricated, Kapton tape is wrapped around the edges of the wafer, thus leaving a free rectangular-shaped area on which the organic semiconductor will be deposited, while simultaneously preventing the creation of a leak path through erratic deposition. The samples are then mounted onto glass slides and held in place with stainless steel alligator clips. Care is taken to avoid contact between the clips' teeth and the oxide to prevent scratching and contamination. For the transistor samples, the clips' teeth rest on the Kapton tape, while for the transmission samples, pieces of Tantalum foil are used.

After the organic semiconductor film has been deposited, a molybdenum shadow mask is placed on the sample, held in place with alligator clips. The mask has 16 pairs of square apertures of different sizes and spatial distribution, representing the footprints of the device contacts. The deposition process is repeated with a new boat containing gold pellets to deposit the contacts of the devices. Table **2.1** shows the channel dimensions and width-to-length ratio of the 16 devices contained in each chip.

Table 2.1: Channel Dimensions

Device	Channel Width (μm)	Channel Length(μm)	Width-to-length Ratio
A1	1638	198	8.27
A2	1089	198	5.5
A3	531	180	2.95
A4	261	178.2	1.46
B1	1620	139.5	11.61
B2	1080	135	8
B3	535.5	130.5	4.1
B4	252	117	2.15
C1	1665	87.3	19.1
C2	1053	81	13
C3	537.3	72	7.43
C4	261	63	4.14
D1	1683	45	37.4
D2	1098	45	24.4
D3	540	40.5	13.3
D4	261	36	7.25

2.2.2 Deposition

The Vacuum Chamber

The deposition takes place in a Denton Vacuum Thermal Evaporator (Figure **2.1**). The deposition chamber consists of a glass bell jar resting on a steel plate with a rubber seal in between. The organic material (either pentacene or HOC6PTTPC6OH) to be deposited on the silicon oxide substrate is placed in a ceramic crucible, which in turn sits in a molybdenum boat attached to conducting arms connected directly to a power supply. The silicon wafer, held to the glass slides by the alligator clips, is placed approximately 14 inches face-down above the crucible. An Al-Cr thermocouple wedged between the crucible and the molybdenum boat measures the temperature of the crucible during deposition, while a second thermocouple is placed near the samples to ensure that they don't overheat during the deposition. A manually turnable shutter located between the sample and the crucible allows the sample to be shielded until

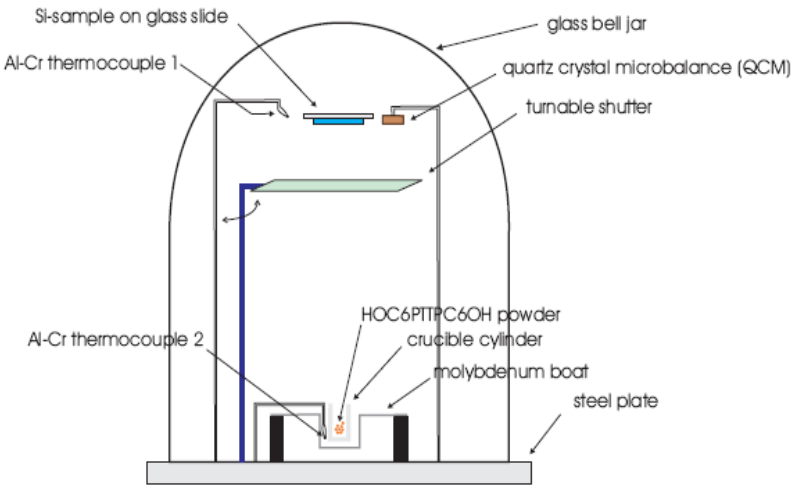

Figure 2.1: Schematic diagram of vacuum evaporation chamber, taken from [38]

the correct deposition parameters are reached.

Once the sample and semiconducting powder are in place, vacuum grease is applied to the rubber O-ring to improve the seal and prevent leaks, and the bell jar is then lowered onto the plate. (The combined pumping action of a turbo pump and a mechanical pump brings the pressure inside the jar to approximately $2 - 4 \times 10^{-6}$ Torr. in about 4 hours). At this point the actual deposition can be started.

Thermal Evaporation through resistive heating

The thermal evaporation of the organic semiconductors and the gold is achieved through ohmic (resistive) heating of the holding boat; i.e. the conversion of electric energy of an alternating high current into thermal energy. Combining Joule's law and Ohm's law, the thermal energy is given by the following equation:

$$P_{therm} = I^2 \cdot R \tag{2.1}$$

where P_{therm} is the thermal energy, I the current and R the resistance. In our

system, all wires and connectors are large cross-section, low-resistance conductors. The boats have a much larger resistance due to their much smaller cross-sectional area (compared to the holding arms and wires) — causing the electrical power of the current flowing through the boats to be much larger. This electrical power is converted into thermal energy, resulting in the heating of the material held within the boat. Since the region with the small cross-sectional area is small compared to the rest of the conductive structure, the heating is concentrated in the boat, with minimal heating of the surrounding areas.

To overcome one of the shortcomings of the evaporator with regard to depositing organic material, we modified it by connecting an external power supply to one of the original evaporator's pairs of conductive arms. Since the evaporator was originally intended to evaporate metals and inorganics onto silicon wafers, it provides good precision for the high currents required for evaporating such materials (typically 100-500 Amps). However, organic semiconductors evaporate at lower temperatures, and therefore require lower currents (typically 50-100 Amps); but the evaporator as it is lacks this precision for the lower ranges required for organic semiconductors . Prior to the addition of this external power supply, the amount of current passed through the boat during organic deposition could not be determined accurately [38]. Thus, it was difficult to achieve stable and reproducible depositions due to the fluctuating deposition rates, and unnecessary loss of material was incurred while the deposition rate was being optimized.

The addition of the external power supply solves this problem, granting a good degree of control over the deposition rate, and allowing the desired deposition rate to be reached faster. Indeed, we have been able to deposit pentacene and HOC6PTTPC6OH at precise rates as planned prior to the experiment run.

Film thickness estimation using Quartz Crystal Microbalance

The thickness of the deposited film is measured using a quartz crystal microbalance (QCM, Inficon), which displays the film thickness with a resolution of 1Å and a constantly updating average deposition rate (over the last 10 seconds) with a resolution of 0.1Å/sec. The QCM was first described by Sauerbrey in 1959 [42]. The basic concept is a quartz crystal vibrating at resonant frequency, and when a thin film of material is deposited on it, the vibration frequency shifts. This shift in the resonant frequency is directly related to the change in mass: $\triangle f \propto K \triangle m$.

The mass sensitivity of the crystal is location-dependant, determined by the acceleration of the crystal vibration at any given point on the crystal [43]. This means that the vibration amplitude, and consequently, the frequency shift is not constant across the crystal. Also, there exists an acoustic mismatch between the crystal and the deposited film. This mandates a compensation procedure, known as z-matching, (inventor unknown), which has been improved by Wajid [44]. This requires that we enter the z-ratio, also known as the acoustic impedance ratio, for each material we are depositing prior to the deposition process.

The QCM provides an average film thickness calculated from the measured mass deposited on the crystal, as well as a deposition rate given at any moment as the average deposition rate over the last 10 seconds.

2.2.3 Post-Deposition

After the deposition is over, the pumps are turned off and the sample allowed to cool. The sample is then removed from the vacuum chamber, and the Kapton tape is removed. A plastic pipette is used to manually scribe lines between the pairs of gold contacts as a means to separate the different devices from one another and confine current flow within the channel of the device being tested.

Following that, a diamond-tipped cutter is used to scratch the silicon oxide and

expose the underlying silicon, thus forming the gate contact onto which a probe will be placed to measure the current flowing the silicon layer. Caution is exercised during this process to expose a sufficient area of silicon while avoiding breaking the sample.

Chapter 3

Electrical characterization of the fabricated devices

3.1 Experimental procedures

3.1.1 Probe Station

The Probe Station is housed in a shielding box placed on a vibration isolation table. The pump which activates the vibration also anchors the probe arms onto the stage. Fine probe tips attach to the probe arms which can be controlled with a fine manipulator. Coaxial cables clip on to the arms and connect to the Semiconductor Parameter Analyzer through the shielding box. The shielding box which acts as a Faraday cage is grounded, and protects the probe station inside from external noise.

The sample is placed on the chuck, and the microscope is maneuvered above the sample using the stage positioners. The lamp is turned on, and the sample is viewed through the lowest magnification objective. Taking care to ensure the probe tips are high enough to clear the sample, the probe arms are turned such that the probe tips are above the sample. Looking through the microscope, the probe tips are moved in the X and Y direction using the fine manipulators and positioned above

the appropriate device. Starting with the gate probe, which is also the thickest, the probes are carefully lowered using the fine manipulator. The tips slowly come into focus as they are lowered, and a small lateral movement is observed once the probe tip has touched the contact. The tips are very delicate, and special care should be taken to avoid bending or breaking them during this process.

After the probes are in position, the lamp is turned off as it could heat up the sample and affect the measurements, and the door on the shielding box is closed in preparation for the electrical measurements.

3.1.2 Electrical Measurements

The electrical measurements were performed using a HP4156 precision semiconductor analyzer (Agilent Technology), which has a current resolution of 1 fA . Typical measurements included ambient current measurements, leakage currents, transfer characteristics (I_{DS} versus V_G) for different drain-sources voltages, and output characteristics, also called I-V plots (I_{DS} versus V_{DS} for different gate voltage values).

Transfer characteristics were calculated by sweeping V_G from 0 to -50 in steps of 1V, while holding V_{DS} constant at -5V, then -20V and looking for the symmetry which reveals the existence (or lack) of current leakage. I-V plots were obtained by sweeping V_{DS} from 0 to -50V in steps of -2.5V, and V_G from to -50 in steps of -10V. From the I-V plots, I_{DS} values were sampled and used to calculate the field effect mobilities.

3.1.3 Field Effect Mobility calculations

The measure of electrical performance for organic thin film transistors is the field effect mobility, μ. This can be calculated by starting with the transistor current equations. Transistors can operate in the linear or saturation mode, and the current in the semiconductor channel (between the source and the drain) equations is given

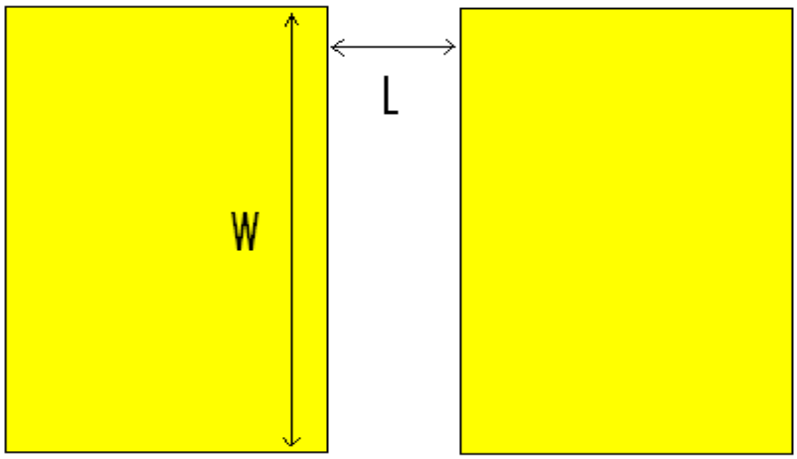

Figure 3.1: Diagram showing width and length of channel

by equations 3.1 and 3.2, respectively; shown below [45]:

$$I_{DSlinear} = \frac{W}{L} \cdot C_i \cdot \mu \cdot V_D(V_G - V_O) \tag{3.1}$$

$$I_{DSsaturation} = \frac{1}{2} \cdot \frac{W}{L} \cdot C_i \cdot \mu \cdot (V_G - V_O)^2 \tag{3.2}$$

where V_O is the threshold voltage, C_i is the capacitance per unit area, given by **equation 3.3**, W is the width, and L is the length, of the channel.

$$C_i = \frac{\kappa \cdot \epsilon_0}{d} \tag{3.3}$$

κ is the dielectric constant ($\kappa_{SiO_2} = 3.9$ [46]), ϵ_0 is the permittivity in space ($8.854^{-12} F/m$), and d is the thickness of the silicon oxide layer, determined to be 1100Å through Rutherford Back Scattering.

Either the linear or the saturation regimes can be used to calculate the field effect mobility. In this thesis, the mobility is calculated in the saturation regime,

and all reference to I_{DS} assume saturation. This is usually obtained by calculating the slope of the best linear fit to $|I_{DS}|^{\frac{1}{2}}$ versus V_G [47]. Usually, the chosen $I_{DS}^{\frac{1}{2}}$ are those along the plotted curve which form a straight line and therefore an optimal fit. Some studies will refer to "well-behaved" $|I_{DS}|^{\frac{1}{2}}$ versus V_G values [26], while numerous others attribute the choice of points to the threshold voltage [48, 49], i.e. the fit to the curve is calculated only for points corresponding to voltages above the threshold. Contrary to regular MOS-FETs, which operate in the depletion mode, and therefore have a clear threshold voltage representing the gate voltage value at which the channel is completely reversed, organic thin film transistors operate in the accumulation mode, and their theoretical threshold voltage is zero [50]. However, in practice, organic thin film transistors do exhibit a threshold voltage; the channel shows no transistor performance below a certain voltage. Consequently, the $|I_{DS}|^{\frac{1}{2}}$ versus V_G is not completely linear, and the points below the threshold voltage are not included in the fit.

The explanation for the presence of this threshold voltage has been attributed to the gate voltage-dependent mobilities that these devices exhibit [49], which in turn is explained by the fact that the high gate voltage induces more charge carriers into the conduction region of the channel resulting in higher currents at higher values. Other studies explain the presence of the threshold voltage by the high resistance exhibited by the gold contact-semiconductor interface [51, 48]. These contacts do not act as truly ohmic contacts, but rather as metal-insulator tunneling type barriers, with combined ohmic charge injection and Fowler-Nordheim tunneling-type injection. The threshold voltage will increase accordingly. Some researchers attempt to lower the resistance of the contacts [52] or change the type of injection barrier (eg. into a Schottky contact barrier) [53] to decrease the injection barrier, and as a result higher mobilities are reported.

Since it has been demonstrated that the threshold voltage is prone to shifting [32,

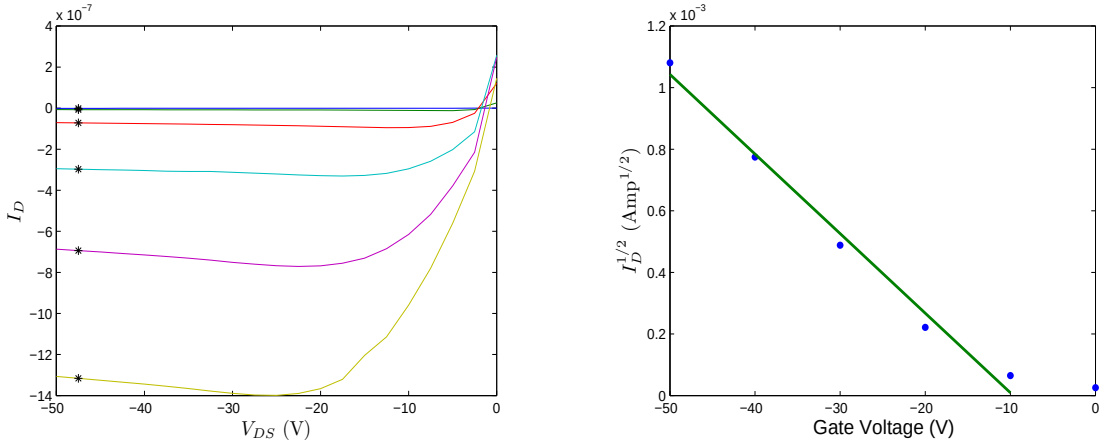

Figure 3.2: Example of plots used for mobility calculation

54], our focus in characterizing the electrical performance was to employ a consistent method for mobility calculation that would readily reveal the performance differences for the various deposition parameters. Since our V_G step in the I-V measurements was somewhat large (-10V), we could not skip many points when calculating the best linear fit for fear of misrepresenting the data. Therefore, we consistently skipped only the V_G=0 point and calculated the best linear fit for the five consequent gate voltage points (from -10V to -50V). For some devices, the linear fit would have been better if we had skipped more points, but we eventually decided against it as that would have resulted in large fluctuations in the threshold voltage for similar devices, with negligible difference in the calculated mobility.

Figure 3.1.3 shows an example of how the mobility values are calculated from the plots described above:

3.2 Results

3.2.1 Quantification of Leak and Ambient Currents

Due to various leakage currents interfering with prior measurements, direct quantification of such currents was deemed necessary. "Ambient" currents are those picked

up by the probes from the surrounding environment, whereas leak currents are those that result from charges tunneling through the oxide layer towards the underlying silicon. To quantify leak currents measurements are run on a device that has no organic semiconducting layer. Instead, the device is fabricated by depositing gold contacts directly on the silicon oxide substrate.

Ambient currents through Probe Station cables

Since these ambient currents represent currents that are picked up by the probes from the surrounding air, rather than the currents flowing through the organic semiconductor film or the silicon, all probes are lifted so that they make no contact with the devices. V_D is set to -5V, and V_G is swept from 0 to -30V in steps of -1V. Figure **3.3** shows currents in the picoamp range in all three probes when they are not in contact with the devices. I_G increases slightly from 0 to -3×10^{-12} Amps, whereas I_D and I_S exhibit seemingly random picoamp fluctuations around zero.

Gate leakage current & the glass slide effect

Since there is no semiconductor film between the gold contacts on our gold-on-oxide device, there is no medium no pass the current resulting from the potential difference between the source and drain. Thus, currents measured by the gate probe are those that have managed to tunnel through the insulating oxide layer to the doped silicon. Placing the sample directly onto the sample holder in the probe station could potentially enhance the gate current leak. To counter this effect, we place a glass slide between the sample and chuck. This places a capacitor in the path of gate current leaking to the chuck, thus eliminating a large portion of this leak.

Figure **3.4** shows a direct comparison of the gate current under the two conditions (without glass slide and with glass slide) for two runs when V_{DS} is set to -5V and V_G

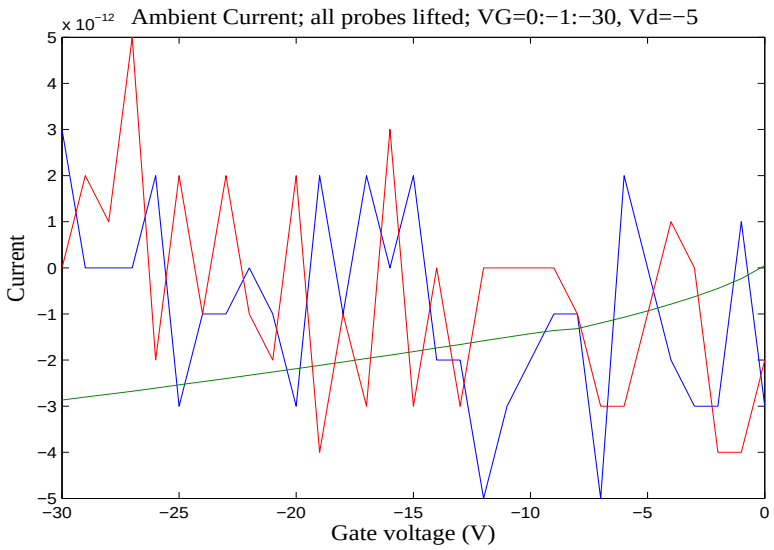

Figure 3.3: Ambient Currents in the picoamp range passing through Source, Gate and Drain Probes that are not in contact with device.

is swept from 0 to -30V in steps of -1V. We can see that the magnitude of the gate current decreases overall after the placement of the glass slide, and is less prone to fluctuations.

3.2.2 Pentacene devices

Having modified the evaporator, we test it by fabricating a pentacene device, with a film thickness 400Å deposited over 31 minutes and 30 seconds, with an average deposition rate of 0.21 Å/sec. **Table 3.1** shows the calculated mobilities for the tested devices in this sample, while **Figure 3.5** shows the I-V characteristics of the tested devices. The highest current was approximately 243 μAmp for V_{DS}=-50V and V_G=-50V. The mean calculated mobility for this pentacene sample is 0.18±0.05 $cm^2V^{-1}s^{-1}$.

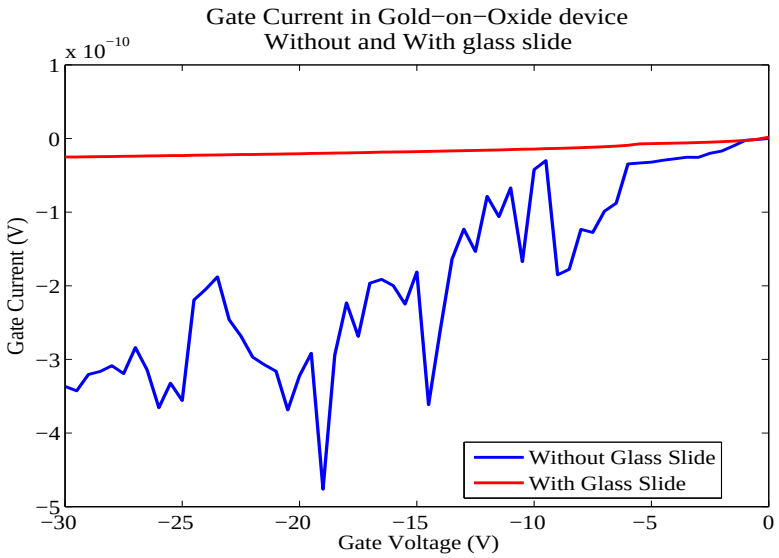

Figure 3.4: Comparison of Gate Leakage currents, showing gate leakage is less with glass slide versus no glass slide.

3.2.3 Initial HOC6PTTPC6OH results

The quality of the HOC6PTTPC6OH batch in use was suspect. The material had been synthesized over a year before these experiments were run. Ongoing work in the group up to this point had shown little or no transistor performance from HOC6PTTPC6OH devices. To determine whether the fault was in the material or in the deposition method, HOC6PTTPC6OH devices were fabricated and tested to see whether they exhibit transistor performance.

Table 3.1: Mobility Values for 400Å Pentacene film deposited at 0.21 Å/sec

Device	calculated mobility ($cm^2V^{-1}s^{-1}$)
A1 (W/L = 8.27)	0.17
B2 (W/L = 8)	0.14
B4 (W/L = 2.15)	0.27
C1 (W/L = 19.1)	0.14
C3 (W/L = 7.43)	0.17
D4 (W/L = 7.25)	0.16

I-V characteristics: 400 Å pentacene film deposited at 0.21 Å/sec

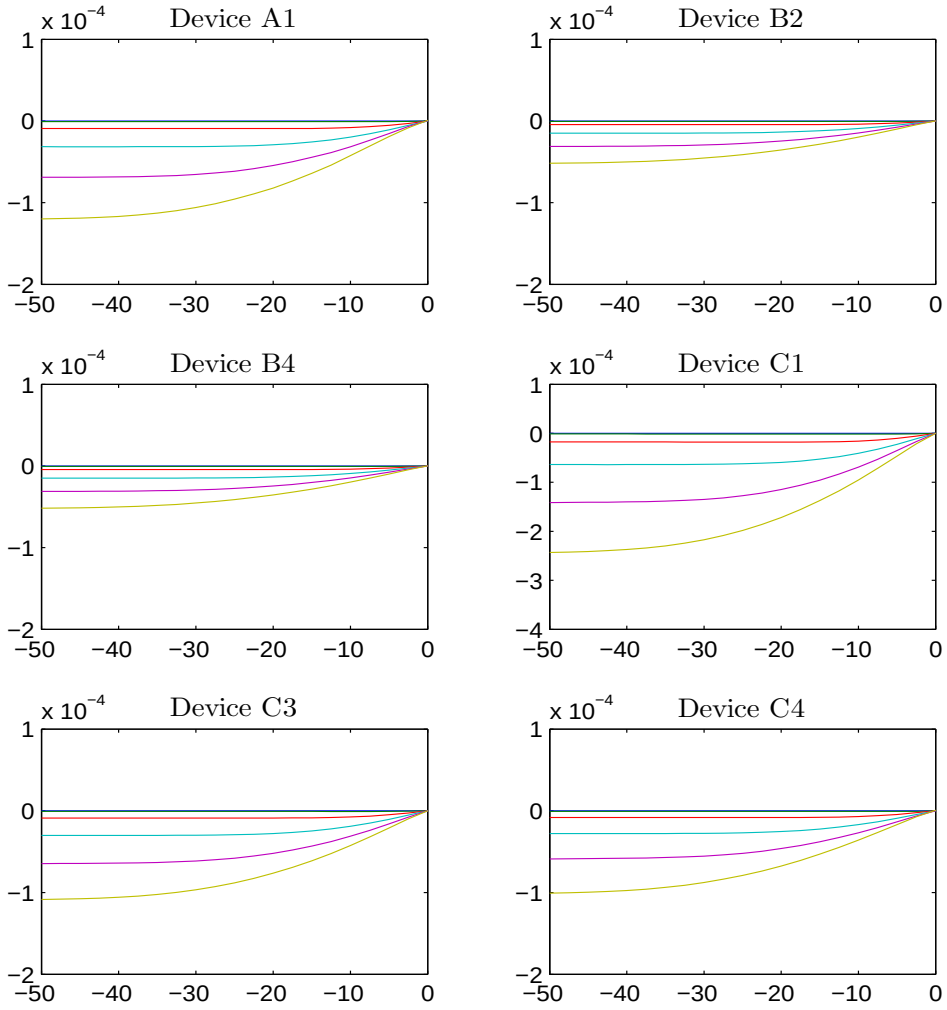

Figure 3.5: I-V characteristics of tested devices on 400Å-thick pentacene film deposited at 0.21 Å/sec.

250Å Film at a low deposition rate

A sample of HOC6PTTPC6OH devices were fabricated by depositing 250Å of HOC6PTTPC6OH at approximately 0.12Å/sec. Drain and source currents in these devices were consistently low (in the nanoamp range). Some devices exhibited saturation, whereas others did not.

Figure 3.6 shows an example of an IV plot obtained from device B3, when V_{DS} was swept from 0 to -50V in steps of -2.5V, and V_G was swept from 0 to -50V in steps of -10V. These values show no transistor performance by the 250 Å film deposited by the current batch at 0.12Å/sec, and therefore no attempt was made to calculate mobilities.

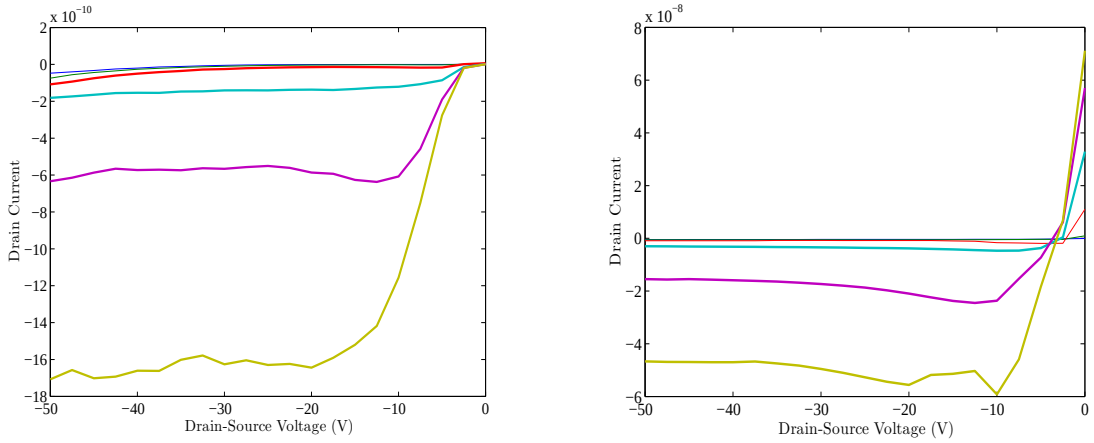

Figure 3.6: Samples of aged HOC6PTTPC6OH device performance showing saturation, although the drain current is in the nanoamp range.

500Å Film at a higher deposition rate

Following that experiment, a second sample was fabricated by depositing a thicker film (500Å) of HOC6PTTPC6OH at a higher rate (0.6 Å/sec). This second set of devices performed a little better; however, these devices did not display smooth I-V

curves, nor did they pass microamp currents.

Figure **3.7** shows an example of this sample's performance. The figure on the left shows the resulting currents when V_G is swept from 0 to -50V in steps of -1V, and V_{DS} is set to -5V, then -20V. For this sample too, no mobilities were calculated, as the performance was deemed unsatisfactory and did not merit further analysis. Note that, for the lower V_{DS} value (V_{DS}=-5), the gate current (leak current) exceeds the drain current.

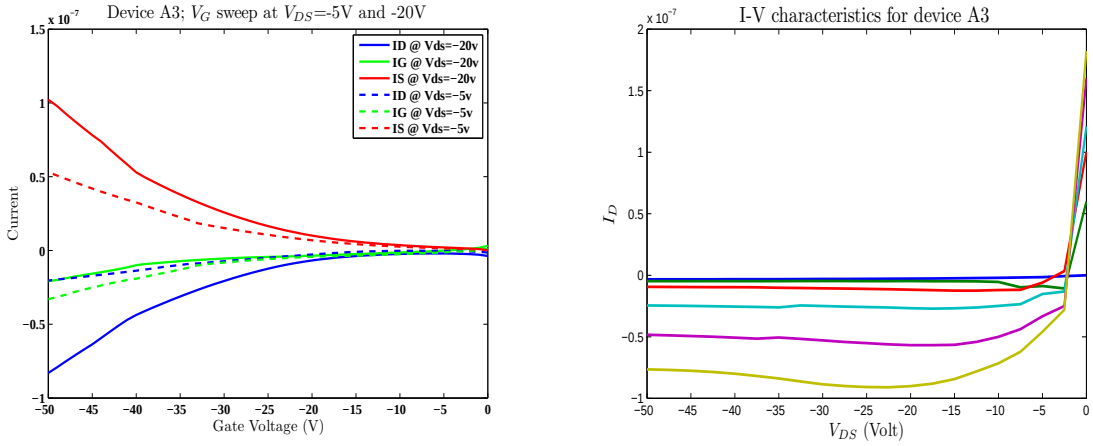

Figure 3.7: Example of better performance of older HOC6PTTPC6OH when deposited in a thicker film.
Left: Currents when V_G swept from 0 to -50V and V_{DS} set to -5V and -20V. *Right*: I-V characteristics.

3.2.4 HOC6PTTPC6OH devices fabricated from a newer batch

Gaining confidence in the precision of the deposition rate that we had been able to achieve, we obtained a newly synthesized batch of HOC6PTTPC6OH from Dr. Ali Afzali at IBM. The results that ensued were much better, i.e. the channel currents were in the microamp range and the calculated mobilities were in the 10^{-2} $cm^2V^{-1}s^{-1}$ range.

The following sections detail the results obtained from devices fabricated with different combinations of deposition rate and film thickness.

250Å HOC6PTTPC6OH Film & low deposition rate

For this sample, 251Å of HOC6PTTPC6OH were deposited over 31 minutes and 25 seconds, yielding an average deposition rate of 0.13 Å/sec. Mobility extraction yielded the mobilities shown in **table 3.2** for the tested devices, while **Figure 3.8** shows recorded I-V characteristics for the tested devices in this sample, demonstrating that these devices, do indeed display transistor performance. The mean mobility for this sample is 0.0017±0.0007 $cm^2V^{-1}s^{-1}$.

Table 3.2: Mobility Values for 250Å HOC6PTTPC6OH film deposited at 0.13 Å/sec

Device	calculated mobility ($cm^2 \cdot V^{-1} \cdot s^{-1}$)
A1 (W/L = 8.27)	0.0018
A3 (W/L = 2.95)	0.0024
B2 (W/L = 8)	0.0018
B4 (W/L = 2.15)	0.0022
C1 (W/L = 19.1)	0.0019
C3 (W/L = 7.43)	0.0019
D2 (W/L = 24.4)	0.0018
D4 (W/L = 7.25)	0.0001

250Å HOC6PTTPC6OH Film & high deposition rate

251 Å of HOC6PTTPC6OH were deposited in 5 minutes and 46 seconds, yielding an average deposition rate of 0.72 Å/sec. The calculated mobilities for the tested devices on this sample are shown in **Table 3.3**. **Figure 3.9** shows that the tested devices exhibit transistor performance; although, device C1 failed — yielding ∼80 μA gate current for the transfer characteristics plot when V_{DS} is set to -5V. The mean mobility for this sample is 0.0022±0.0007 $cm^2V^{-1}s^{-1}$.

I-V characteristics: 250 Å HOC6PTTPC6OH film deposited at 0.13 Å/sec

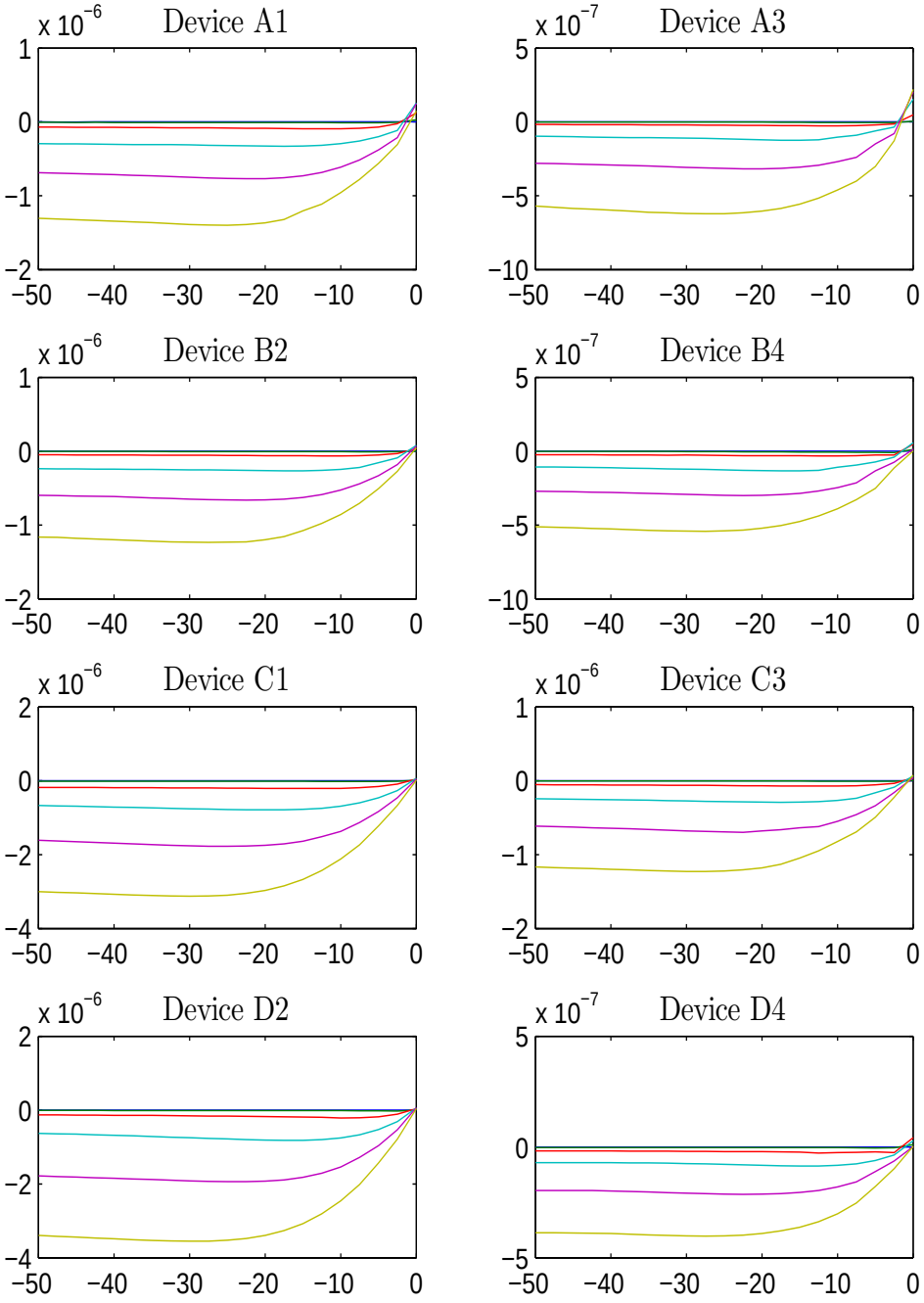

Figure 3.8: I-V characteristics of tested devices on 250Å thick film deposited at 0.13 Å/sec.

I-V characteristics: 250 Å HOC6PTTPC6OH film deposited at 0.72 Å/sec

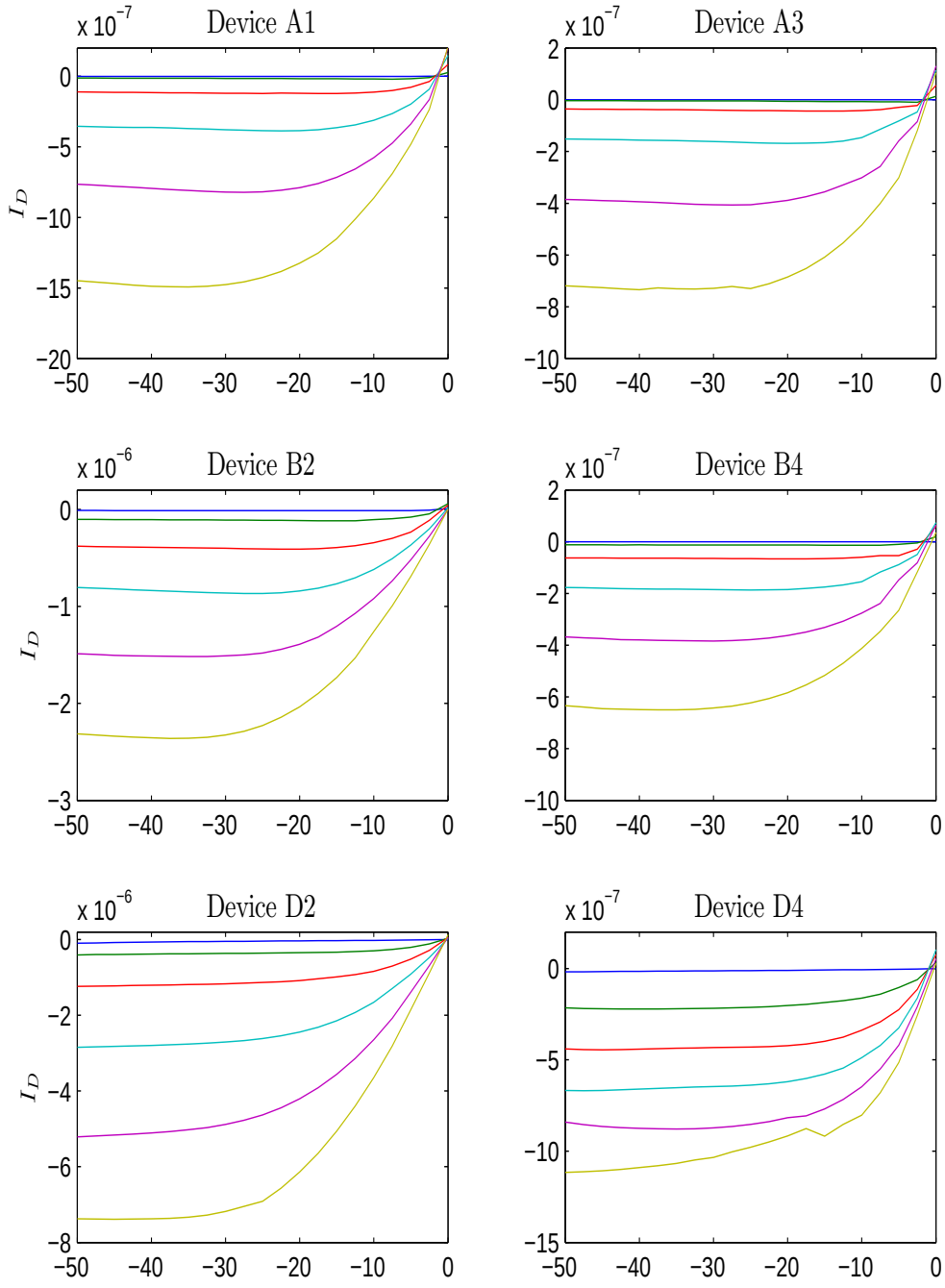

Figure 3.9: I-V characteristics of tested devices on 250Å thick film deposited at 0.72 Å/sec.

Table 3.3: Mobility Values for 250Å HOC6PTTPC6OH film deposited at 0.72 Å/sec

Device	calculated mobility ($cm^2V^{-1}s^{-1}$)
A1 (W/L = 8.27)	0.0019
A3 (W/L = 2.95)	0.0029
B2 (W/L = 8)	0.0024
B4 (W/L = 2.15)	0.0024
C1 (W/L = 19.1)	Bad device
D2 (W/L = 24.4)	0.0025
D4 (W/L = 7.25)	0.0009

500Å HOC6PTTPC6OH Film & low deposition rate

502 Å of HOC6PTTPC6OH were deposited over 45 minutes and 54 seconds, yielding an average deposition rate of 0.18 Å/sec. The calculated mobilities for the tested devices are displayed in **Table 3.4**, and the I-V characteristics for these devices are shown in **Figure 3.10**. The mean mobility for this sample is 0.0017±0.0009 $cm^2V^{-1}s^{-1}$.

Table 3.4: Mobility Values for 500Å HOC6PTTPC6OH film deposited at 0.18 Å/sec

Device	calculated mobility ($cm^2 \cdot V^{-1} \cdot s^{-1}$)
A1 (W/L = 8.27)	0.0010
A3 (W/L = 2.95)	0.0035
B2 (W/L = 8)	0.0016
B4 (W/L = 2.15)	0.0026
C1 (W/L = 19.1)	0.0007
C3 (W/L = 7.43)	0.0012
D2 (W/L = 24.4)	0.0013
D4 (W/L = 7.25)	0.0019

500Å HOC6PTTPC6OH Film & high deposition rate

500 Å of HOC6PTTPC6OH were deposited over 10 minutes and 25 seconds, yielding an average deposition rate of 0.8 Å/sec. **Table 3.5** shows the calculated mobilities for the tested devices, while **Figure 3.11** shows their I-V characteristics. Device D4 did

I-V characteristics: 500Å HOC6PTTPC6OH film deposited at 0.18 Å/sec

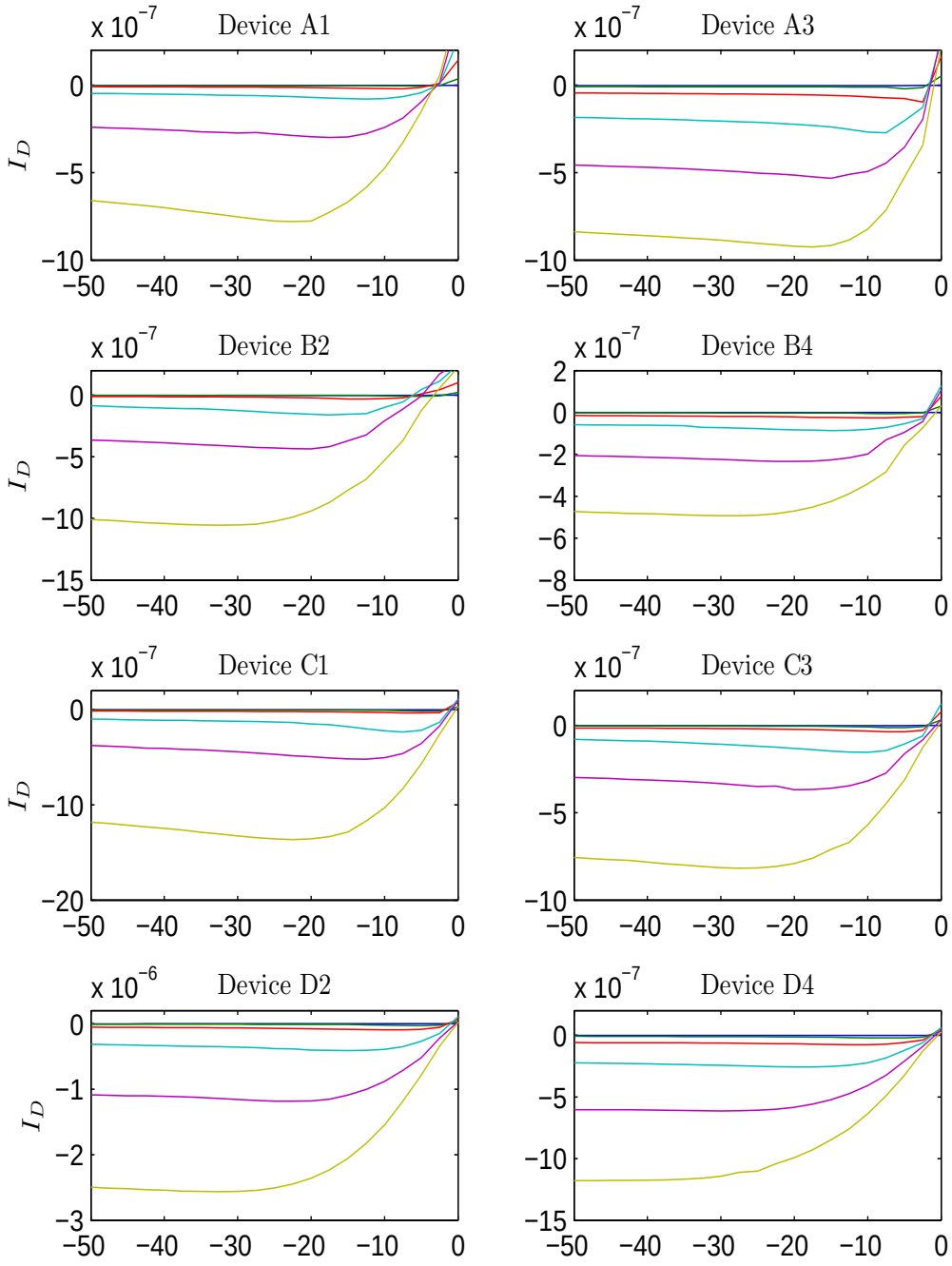

Figure 3.10: I-V characteristics of tested devices on 250Å thick film deposited at 0.18 Å/sec.

not exhibit transistor performance, but rather linear currents with respect to voltage, and was therefore not included in the mobility calculations. The mean mobility for this sample was $0.0023 \pm 0.0008 cm^2 V^{-1} s^{-1}$.

Table 3.5: Mobility Values for 500Å HOC6PTTPC6OH film deposited at 0.8 Å/sec

Device	calculated mobility ($cm^2 \cdot V^{-1} \cdot s^{-1}$)
A1 (W/L = 8.27)	0.0027
A3 (W/L = 2.95)	0.0009
B2 (W/L = 8)	0.0024
B4 (W/L = 2.15)	0.0036
C1 (W/L = 19.1)	0.0020
C3 (W/L = 7.43)	0.0023
D2 (W/L = 24.4)	0.0020

I-V characteristics: 500Å HOC6PTTPC6OH film deposited at 0.8 Å/sec

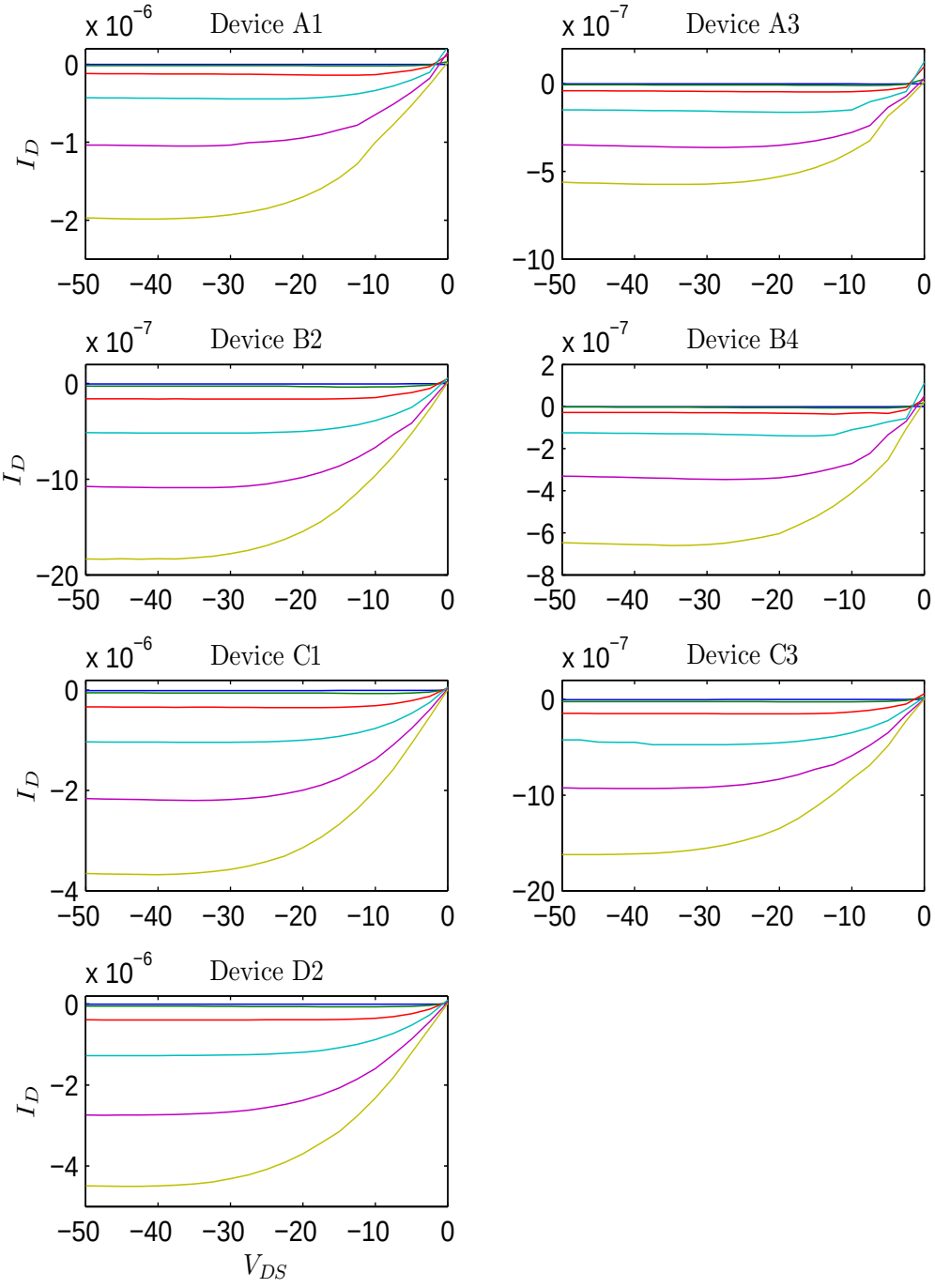

Figure 3.11: I-V characteristics of tested devices on 250Å thick film deposited at 0.8 Å/sec.

Chapter 4

Topological characterization of the deposited films using Atomic Force Microscopy

4.1 AFM principles

Atomic Force Microscopy is a useful method to discern the topography of a surface with nanometer resolution, developed by Binnig et al. in 1986 [55] . Unlike traditional microscopy techniques which use electromagnetic radiation (photon or electron beams) to create an image, atomic force microscopy is a mechanical technique that measures the three-dimensional properties of a surface by scanning it with a sharp probe. This is accomplished by using a cantilever ending with a sharp tip (fabricated using micromachining techniques) positioned close enough to the surface of the sample to interact with the force fields associated with the sample [56]. This generates a force F_{ts} between the tip and the sample, and depending on the mode of operation, the AFM uses F_{ts} or other quantities derived from F_{ts} as the imaging signal. This force changes as topology of the surface —and consequently the distance between the tip

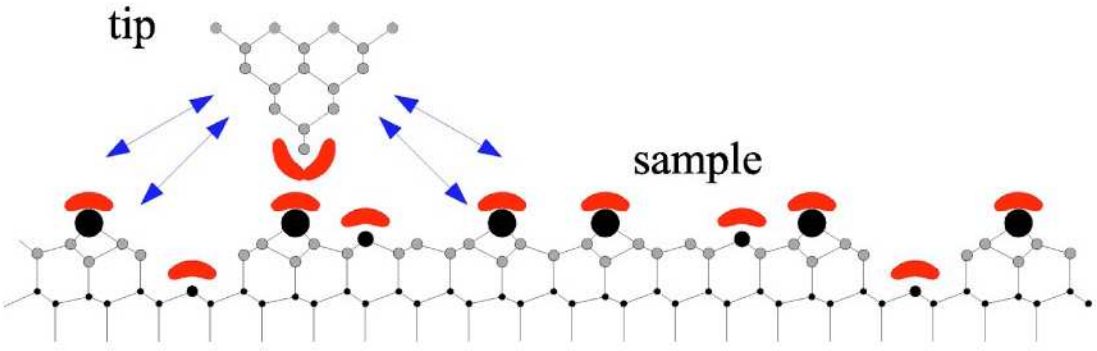

Figure 4.1: Schematic of AFM tip close the sample surface showing forces generated by the overlap of tip and sample orbitals. (Taken from [59])

and the surface— changes, causing the cantilever to deflect. **Figure 4.1** [59] shows a schematic of an AFM tip close to the sample surface. The forces are generated when the tip and sample atom orbitals overlap.

The cantilever is mounted onto an X-Y-Z scanner made of a piezoelectric ceramic capable of moving the probe with subatomic precision. A force transducer measures the force between the tip and the sample; in our case, a light lever sensor is used. In such a transducer, a laser beam is reflected off the backside of the cantilever onto a photo-detector. When the cantilever interacts with the surface, the path of the reflected light will change. The force is measured by measuring the change in the light entering the detector. It is geometrically calculated that the motion of the of the light beam across the detector is equal to the deflection of the parabolic end of the cantilever, and therefore the light beam should be reflected off the parabolic end of the cantilever. A feedback controller maintains a constant force between the probe and the surface by using the output of the light sensor to control the piezoelectric ceramic.

The probe is scanned in the X-Y direction, line by line in a raster fashion, while F_{ts} is monitored and used to generate the imaging signal and the input to the Z motion generator. In these experiments, the AFM is operated in close contact (CC)

vibrating mode, where the probe is vibrated at its resonance frequency. The resonant frequency is given by the following equation [57]:

$$\omega_o = \sqrt{\frac{k_{eff}}{m_{eff}}} \tag{4.1}$$

where k_{eff} is the effect spring constant of the cantilever, and m_{eff} the effective mass . The phase shift at the resonance frequency is 90 degrees. As the probe interacts with the surface the resonance frequency shifts, and phase shift changes correspondingly. The feedback electronics respond to this change, controlling the piezoelectric ceramics to keep the phase shift constant.

Since AFM probes are very delicate, a "woodpecker" approach method is employed to get the probe to the correct proximity to the surface. This typically involves a stepper motor with a resolution of a few microns, in addition to the Z ceramic motion generator. The stepper motor is lowered by a small increment (e.g. 1 μm), then Z piezoelectric ceramic is extended by 5 μm to check if the probe has reached the surface. If not, the Z ceramic is then retracted and the stepper motor is engaged again and lowered by another 1 μm and so on. The feedback controller is turned on as soon the probe encounters the surface.

Atomic force microscopy was chosen over scanning tunneling microscopy (STM) for a variety of reasons. STM can only image conductive materials because it relies on the tunneling current which flows between the biased tip and the sample. Additionally, STM has to be operated under ultra-high vacuum to avoid the effects of the contamination layer, and needs rigorous sample preparation. In contrast, AFM needs no sample preparation and can operate in ambient conditions.

4.2 AFM experimental procedure

A special software (SPM Cockpit, Pacific Nanotech) is used to operate the AFM. First, the correct probe configuration is loaded according to the chosen operation mode. The sample is then loaded onto the holder, and a linearity test is performed to find the full dynamic voltage range and the linear region of this range. The correct mode is selected, and the laser aligned using the laser positioning knobs such that the laser beam is positioned on the parabolic end of the cantilever, and its intensity is above the minimum value set by the software. The probe is then tuned to find the resonance frequency.

The *Stage* window allows access to the AFM's X-Y motor and its optical microscope's objective, which are used to focus on the desired part of the sample. This window also allows a coarse approach of the tip to the sample in preparation for the "woodpecker" fine approach. Once both approaches are complete, the feedback parameters can be altered to optimize the scanning process. The sample can then be scanned in earnest. We first scan a 40 μm $\times$ 40 μm area at resolution of 256$\times$256 pixels and a scan rate of 1 Hz to gain an idea of the topography of the region in question, then zoom in to 20 μm $\times$ 20 μm area at a 512$\times$512 pixels and a 0.7 Hz scan rate to get finer details.

Once the scan is finished, the tip is retracted and the sample removed. The resulting image is processed by leveling to remove global tilts and curvatures, and histogram correction and frequency spectrum correction to remove noise.

4.3 AFM Results

For all films, a $40\mu m \times 40\mu m$ square is first scanned at a low (256$\times$256 μm) with a scanning frequency of 1 Hz to determine the general topology and grain size and

make sure there are minimal artifacts, from dust particles or otherwise. If the result is satisfactory, showing distinct grains and minimal artifacts, we zoom in to a smaller area —$20\mu m \times 20\mu m$— and the scan is repeated at a higher resolution (512×512) and lower frequency (0.7 Hz). Following the image processing steps described in the procedural section, one further processing step is performed with Nanorule. This involves thresholding the image to half the maximum intensity level, thereby isolating the individual grains separated by grooves deeper than midpoint intensity level. The width, length and area of these grains is calculated and used to generate plots to aid in the analysis of film topology. A deeper analysis of the film topology and a comparison between the different films is presented in Chapter 5.

4.3.1 250Å Film & low deposition rate

A three dimensional rendering of the topology of the 250Å film deposited at the low rate, obtained using AFM, is shown in **Figure 4.2**. Performing a grain analysis by thresholding to 28.6 nm, we obtain the number of grains higher than the threshold within the imaged $20\mu m \times 20\mu m$ square of the film, and can calculate the length and width of these grains. A scatter plot of the extracted width and length values is shown in **Figure 4.3** , showing a significant number of grains with dimensions greater than $2\mu m \times 2\mu m$.

The average grain width is 1.6±1.4 μm, and the average grain length is 3±2.5 μm. The maximum grain height is 57.26 nm, and the midpoint is 28.6 nm, which is within 14% of the average film thickness of 250 Å.

4.3.2 500Å Film & low deposition rate

A 3D rendering of the topology of this film is shown in **Figure 4.4**. By thresholding the z (height) values to 53.24 nm, identified grains are identified and their dimensions are obtained. Plotting the length vs. width of the determined grains, we get the plot

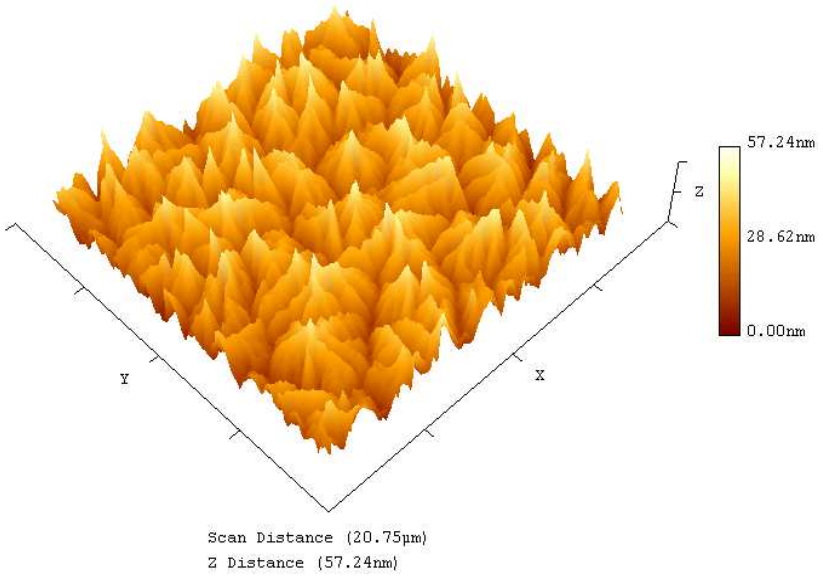

Figure 4.2: 3D rendering of AFM image of a $20\mu m \times 20\mu m$ area of a 250Å-thick HOC6PTTPC6OH film deposited at 0.13 Å/sec.

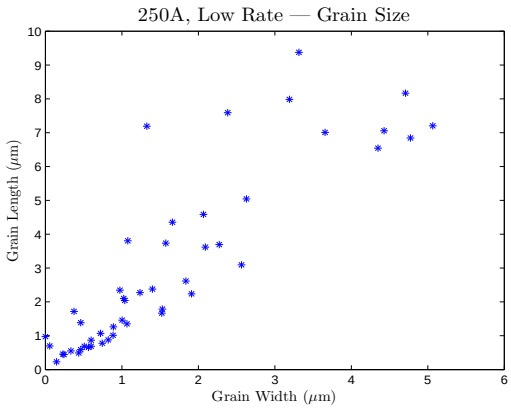

Figure 4.3: 250Å, low rate film: scatter plot showing Grain Width vs. Grain Length.

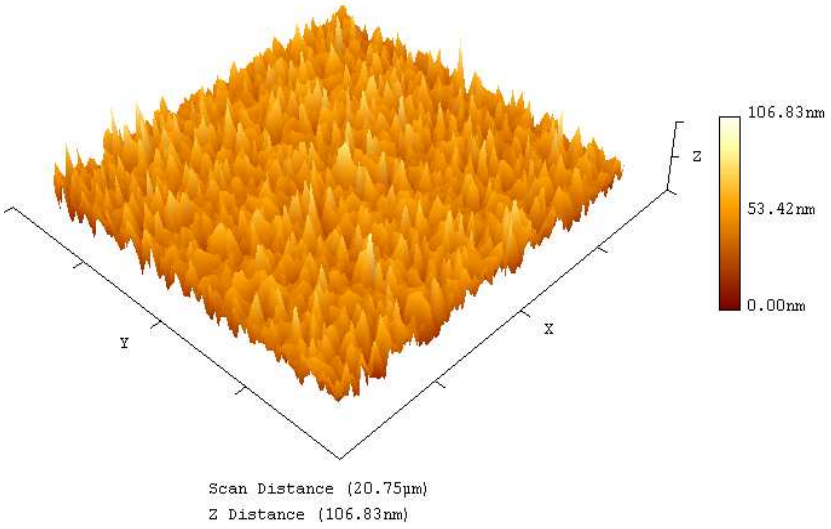

Figure 4.4: 3D rendering of AFM image of a $20\mu m \times 20\mu m$ area of a 500Å-thick HOC6PTTPC6OH film deposited at 0.13 Å/sec.

shown in **Figure 4.5**, which shows an increase in the number of grains, mostly in the sub-$2\mu m \times 2\mu m$ range. There still is a significant number of grains larger than $2\mu m \times 2\mu m$, with the maximum grain size remaining the same as for the 250 Å film deposited at the low rate.

The average grain width is 1 ± 0.96 μm, and the average grain length is 2.1 ± 2.1 μm. The maximum grain height is 106.83 nm, and the midpoint was 53.24 nm. This is within 6.5% of the average film thickness of 500 Å.

4.3.3 250Å Film & high deposition rate

Figure 4.6 shows a 3D rendering of the topology of the 250 Å-thick film deposited at 0.8 Å/sec. For the grain analysis, the height threshold is set to 39.51 nm and the individual grains are determined and their dimensions measured. **Figure 4.7** shows a scatter plot of the width vs. length of the grains. Looking at this plot, we see that the majority of the grains are smaller than $2\mu m \times 2\mu m$.

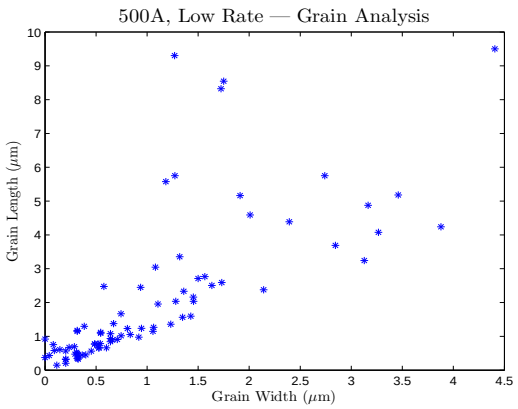

Figure 4.5: 500Å, low rate film: scatter plot showing Grain Width vs. Grain Length.

The average grain width is 0.7±0.5 μm, and the average grain length is 1.1±0.9 μm. The maximum grain height under this condition is 79 nm, and the midpoint is 39.51 nm, which is 58% greater than the average film thickness of 250 Å.

4.3.4 500Å Film & high deposition rate

Figure 4.8 shows the topology of the 500Å film deposited at 0.8 Å/sec. For the grain analysis, the threshold is set to 44.34 nm, and the resulting grain dimensions are plotted in **Figure 4.9**. We can clear see that, except for a few outliers, all the grains are smaller than $1\mu m \times 1\mu m$.

The average grain width is 0.3±0.1 μm, and the average grain length is 0.5±0.2 μm. The maximum grain height is 88.67 nm, and the midpoint is 44.34 nm, which is 11% *less* than the average film thickness.

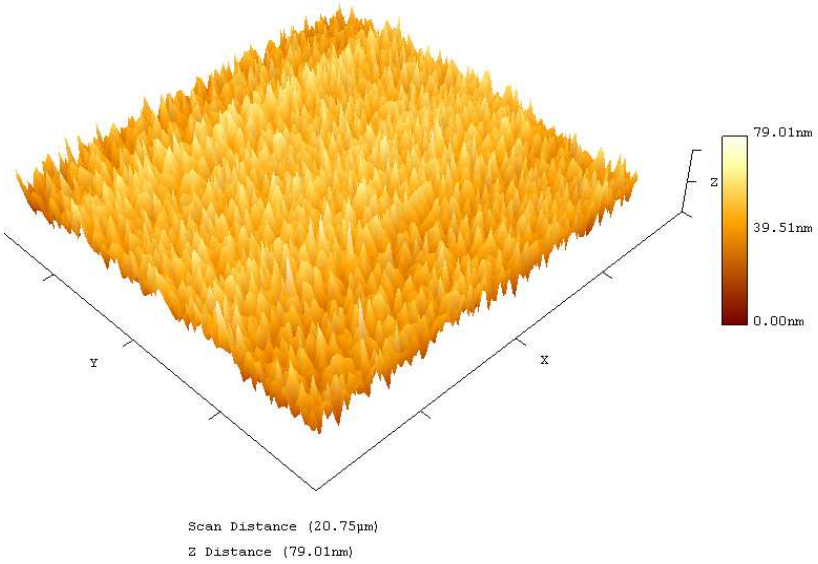

Figure 4.6: 3D rendering of AFM image of a $20\mu m \times 20\mu m$ area of a 250Å-thick HOC6PTTPC6OH film deposited at 0.8 Å/sec.

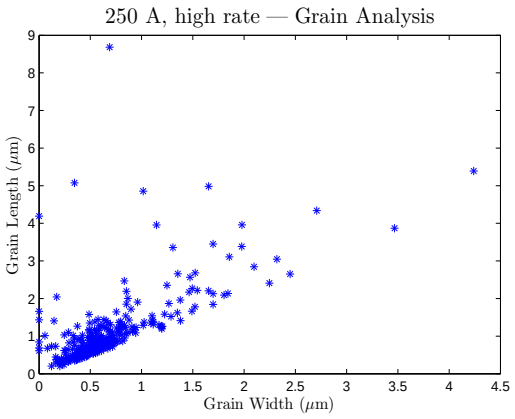

Figure 4.7: 250Å, high rate film: scatter plot showing Grain Width vs. Grain Length.

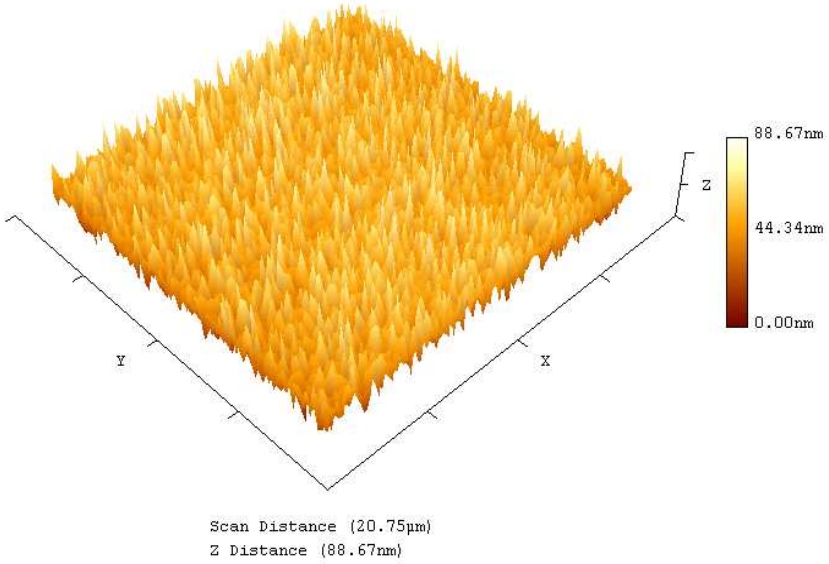

Figure 4.8: 3D rendering of AFM image of a $20\mu m \times 20\mu m$ area of a 500Å-thick HOC6PTTPC6OH film deposited at 0.8 Å/sec.

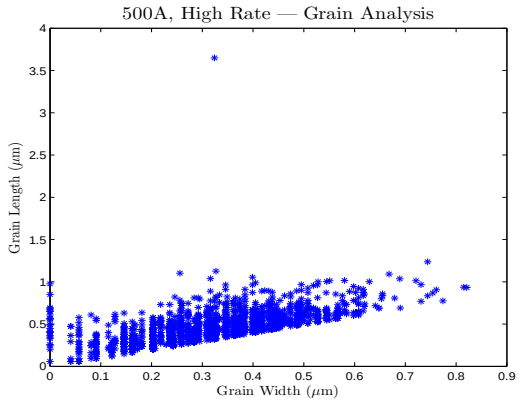

Figure 4.9: 500Å, high rate film: scatter plot showing Grain Width vs. Grain Length.

Chapter 5

Discussion

This section will show a side-by-side comparison of the calculated mobilities and the film topology for the different deposition conditions. Each of the deposition parameters (the rate and the film thickness) will be discussed with relation to its effect on electrical performance and grain size. From there, an attempt to correlate the electrical and topological characteristics of the fabricated films will be made.

Table 5.1 shows the mean calculated mobilities for the different samples. We can see that the deposition rates that we employed in this experiment affect the obtained mobility values, as the higher deposition rate employed resulted in a 32% increase in mobility as compared to the lower deposition rate. The thickness, however, has no noticeable effect on the calculated mobility value. The films of different thicknesses deposited at the same rate exhibit the same mobility value (within the range of error).

Figure 5.1 presents the AFM images of the obtained by scanning the samples deposited at the different combinations of film thickness and deposition rates. By qualitatively looking at the images, we see the AFM image for 250Å low rate film exhibits the largest grains, followed by the 500Å low rate film, then the 250Å high rate film and finally the 500Å high rate film.

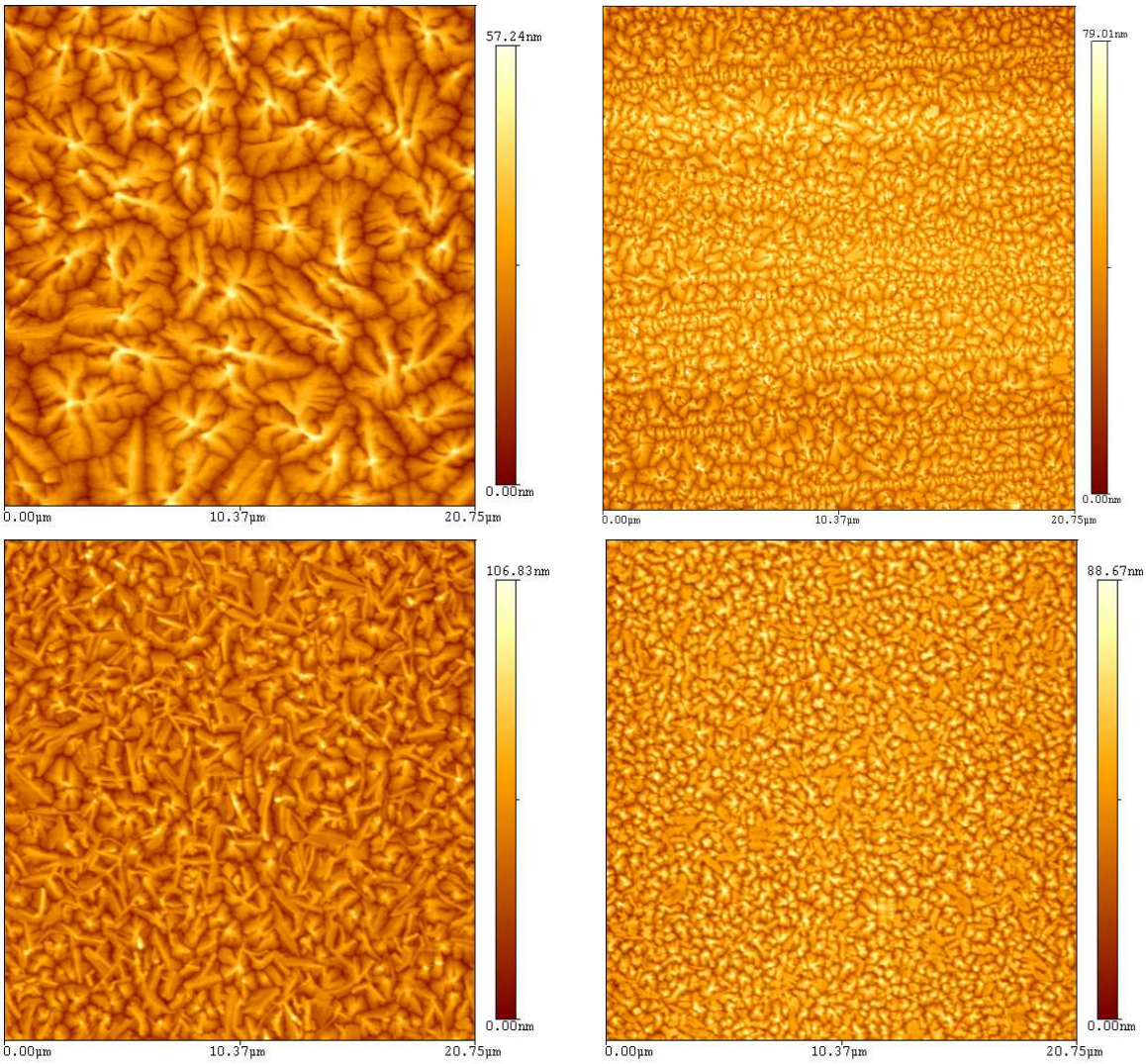

Figure 5.1: 2D AFM images of the different tested HOC6PTTPC6OH films

Top Left: 250Å, Low Rate
Top Right: 250Å, High Rate
Bottom Left: 500Å, Low Rate
Bottom Right: 500Å, High Rate.

Table 5.1: Mean mobility values for different films ($cm^2V^{-1}s-1$)

	Low Rate	High Rate
250 Å	0.0017±0.0007	0.0022±0.0007
500 Å	0.0017±0.0009	0.0023±0.0008

5.1 The effect of film thickness on device performance and grain size

The effect of organic semiconductor film thickness on the calculated field effect injection is a debated issue. While our experiment shows no noticeable relation between the film thickness and the calculated mobilities, other studies have shown that the film thickness can influence the mobility values. Singh et al. demonstrated that there is a non-linear decrease in field effect mobility of Poly(3-hexylthiophene) films when their thicknesses decrease [58], meaning that thicker films give rise to devices with higher mobilities. A contradicting result is presented by Schrœder at al. [53] , where pentacene films are shown to exhibit lower field effect mobilities as the film thickness increases.

However, the deposition rate in Schrœder's experiments is not constant; The different films described were deposited under different rates, ranging between 3 and 7 Å/sec, although which rate was used to deposit which film was not specified. A logical assumption would be that a faster rate was used to deposit the thicker film in order to shorten the fabrication time. This was not discussed in that paper, but could have had an adverse effect on the film structure and consequently on the mobilities of the films. Another factor that could contribute to the apparent difference in the mobility and thickness relation is the different material used in the two experiments.

With regard to the relationship between film thickness and grain size, we can see that both fabrication parameters affect the grain size. For either deposition rate, we

observe (laterally) larger grains in the thinner film. Stadlober et al. [28] argue that for pentacene films increasing in thickness, it is vertical, rather than lateral, grain growth which is responsible for the transition from thin film to bulk phase. Although not relevant for the film thicknesses that we are testing, this phenomenon may explain why the thicker films exhibit smaller grains than the thinner films.

5.2 The effect of deposition rate on device performance and grain size

From Table 5.1, we can see that the two different tested deposition rates resulted in different mobilities; the higher deposition rate resulted in higher mobilities. The deposition rate also had a visible effect on the lateral size of the grains: for two films of the same thickness, the one deposited at the lower rate has markedly larger grains. Pratontep et al. [29] and Stadlober et al. [28] have shown that lower deposition rates result in larger grains, which agrees with our findings. They also report that higher deposition rates results in higher coverage, more compact grain morphology and a higher density of grains of smaller size. This is attributed to the fact that for low deposition rates, the molecules tend to diffuse on the substrate and aggregate in larger islands due to the low nucleation density. Another factor that could affect grain size is the substrate type and the purity of the substrate surface. In a different paper [60], Pratontep et al. describe treating the SiO_2 substrate with oxygen plasma under vacuum prior to the deposition. Our cleaning protocol involved only solvent cleaning for new samples, and piranha for some reused samples that we tested.

However, Stadlober displays results where higher mobilities are linked to lower initial deposition rates, and Pratontep speculates that the larger grains resulting from low deposition rates will display higher mobilities. This contradicts with our findings, where a higher deposition rate resulted in higher mobilities. This discrepancy will be

addressed in the following section.

From the AFM experiments we can see that deposition rate does influence the size of the grains, as was observed from the transmission samples, forming larger grains with pronounced dendrites in films deposited at lower rates.

5.3 The relation between device performance and grain size

The mere presence of larger grains in the deposited films is no guarantee of higher field effect mobilities. In the films presented above, the films deposited at higher rates and consisting of smaller grains exhibited higher mobility values. The film thickness for the different samples did not seem to play an important role in improving the calculated mobility values. As discussed above, mobility values are expected to be higher for lower deposition rates. However, the studies that showed these results employed very low deposition rates, in the range of 0.05Å/sec. This kind of deposition rate is much lower than we were able to accurately provide, due to equipment limitations — the QCM used in these experiments had a rate resolution of 0.1 Å/sec.

However, it has been shown that higher deposition rates result in higher coverage of the substrate. This has been discussed in literature as a disadvantage, due to the increase in grain boundaries that could contribute to charge carrier trapping. In our experiment however, the low deposition rate might not have been low enough to allow the island to fuse at the semiconductor-dielectric interface and therefore the gaps between the grains at this interface might be more than in the case of the films deposited at the higher rate. Since the charge conduction in organic thin film transistors occurs in the one or two monolayers closest to the dielectric surface [61, 25], it is important to have the maximum possible substrate surface coverage with the organic semiconductor. As Stadlober [28] showed, pentacene devices showed the

best mobilities in relation to initial deposition rates of around 0.06 Å/sec, which corresponded to large grain formation, but also to better two dimensional coverage in the sub-monolayer range. The issue of complete monolayer coverage is more important than the grain size with regard to achieving high mobilities as it has been shown that charge transport efficiency transport is adversely affected by interfacial discontinuity in the organic semiconductor film [62]. Since we could not reliably achieve such low deposition rates, it is possible that there discontinuities between the grains in our films that act as charge carrier traps and lower the mobility of the devices, regardless of the apparent size of the grains. This phenomenon could explain why we obtained higher mobilities for the films deposited at the higher rate.

Traps can be induced thermally as shown by DeLongchamp [63], and manifest as changes either in the crystal lattice or the larger grain structure (eg. by cracking). This results in a decrease in mobility corresponding to the formation of a defect in the submonolayer coverage. Additionally, charge carrier traps could be due to molecular interaction and ordering and chemical impurities. Operating TFTs in air, as in the conditions of these experiments, is a cause for special concern because of the susceptibility of organic semiconductor films to oxidative doping and degradation [54].

Studies have been undertaken on pentacene to achieve the initial monolayer formation on the dielectric substrate. One approach, described by Knipp et al., is to coat the SiO_2 substrate surface with a self assembled monolayer of Octadecyltrichlorosilane (OTS) [64] to allow for better attachment of pentacene to the dielectric, yielding a 2-3 times increase in mobility. This method is not foolproof, and mobility fluctuations were observed that were attributed to problems with the monolayer formation. Another approach, described by Sheraw et al., [65] is functionalize the pentacene with bulky functional groups that would prevent edge-to-face interactions and promote improved molecular ordering, and consequently higher π-orbital overlap.

Another procedure that has been applied in organic thin film transistor fabrication

with success in increasing the field effect mobility is to heat the substrate during deposition [30, 26, 31] or rapid thermal annealing immediately after the deposition of the organic semiconductor [52]. This has no effect on the size of the formed grains, but could improve molecular packing within the crystals and result in higher mobilities.

5.4 Implications for gas sensor design

As discussed in the previous section, it is important to achieve maximum monolayer coverage in the semiconductor-dielectric interfacial layer in order to reached the highest potential field effect mobility for poly-crystalline HOC6PTTPC6OH films. Even though it is possible to achieve higher mobilities by attempting to grow single-crystal films of HOC6PTTPC6OH, from a vapor sensing viewpoint it is an advantage, rather than a drawback, to have disjointed grains separated by pits that allow the analyte vapor access to the conduction region (as described in 1.2.3). The devices fabricated and tested in this study produced saturation currents of few microamperes. Devices based on different organic semiconductors, but with saturation currents in the same range as we obtained, have been used successfully to sense a variety of gaseous analytes [9]. Further experiments based on this investigation will involve *in situ* IR spectroscopy on similar devices under exposure to gas vapors. This will advance our understanding of the exact mechanism by which the gases interact with the film surface, and help design better, more sensitive sensors.

Apart from depositing the films at very low deposition rates to achieve maximum coverage at the sub-monolayer level, several procedures can be investigated to improve the mobility of the fabricated devices while preserving the polycrystalline structure of the films with its potential for vapor sensing, in such a way that will reduce noise. These steps can include:

- Depositing the HOC6PTTPC6OH material onto uniformly heated substrates

(85-100 degrees Celsius) instead of room-temperature substrates.

- Applying a self assembled monolayer of a suitable molecule to the SiO_2 surface prior to the HOC6PTTPC6OH deposition. The molecule has to be chosen such that it will interact with the hydroxy terminus on the HOC6PTTPC6OH.

- Functionalization of the HOC6PTTPC6OH molecules with functional groups that would promote better molecular ordering. Even though previous FTIR studies on HOC6PTTPC6OH show that the molecules deposit mostly perpendicular to the surface [38], and thus the $\pi - \pi$ stacking direction is thought to be optimal, HOC6PTTPC6OH might also benefit from the same functionalization process that yielded higher mobilities for pentacene, even when studies show that vacuum deposited pentacene exhibits good molecular ordering and its molecules are perpendicular to the substrate interface. It should be noted that there is a risk of the functional groups acting to prevent the interaction of the analyte molecules with the HOC6PTTPC6OH, or act as a barrier to charge carrier trapping by the analyte molecules.

Chapter 6

Summary

5-5′-bis-4-(6-hydroxyhexyloxy)-phenyl-2-2′-bithiophene (HOC6PTTPC6OH) is proposed as a suitable organic semiconductor for use in vapor sensing applications. Modifications to the existing equipment were made to facilitate organic deposition under well controlled conditions, including the installation of an external power supply with an output more suited for the evaporation of organic materials. Thermal vacuum evaporation was then used to fabricate arrays of thin film transistors with HOC6PTTPC6OH channels at different deposition rates and thicknesses. Pentacene devices were also fabricated as a benchmark for performance. Electrical characterization of the fabricated transistors has been performed, showing that HOC6PTTPC6OH devices consistently display transistor performance for the different fabrication parameters. The calculated field effect mobilities were in the 10^{-3} $cm^2V^{-1}s^{-1}$ range; well below the 10^{-1} $cm^2V^{-1}s^{-1}$ range obtained from pentacene transistors, but still deemed adequate for vapor sensing applications. The rate of deposition of the HOC6PTTPC6OH on the substrate had a visible effect on the calculated mobilities, whereas the thickness of the deposited film did not; there was a 32% increase in mobility when a deposition rate of ∼0.8Å/sec. was employed instead of ∼0.8Å/sec. Atomic Force Microscopy (AFM) was performed on HOC6PTTPC6OH

films without gold contacts, deposited concurrently with the transistor samples. AFM showed that lower deposition rates resulted in larger grains whereas higher deposition rates resulted in smaller grains. Contrary to results presented in literature, the grain size did not show any effect on the field effect mobility. It is hypothesized that the initial monolayer responsible for the majority of the charge carrier conduction suffers surface coverage deficiencies, resulting in discontinuities between the film grains which adversely affect the mobility. It is proposed that the deposition rates used are not low enough to allow a low nucleation density and consequently a complete monolayer formation, and the higher deposition rate resulted in increased initial layer coverage, and therefore higher mobilities . Possible modifications to the deposition process are discussed, including depositing the organic semiconductor onto heated substrates, functionalization of the substrate to facilitate better coverage at the initial monolayer level, and functionalization of the HOC6PTTPC6OH molecule to allow better molecular structure in the film. These steps are suggested with emphasis on keeping the polycrystalline structure in the film as it is hypothesized to produce a stronger sensing response to gaseous, and other biological, analytes than a single crystal morphology.

Bibliography

[1] K. Marx et al. A quartz crystal microbalance cell biosensor: Detection of microtubule alterations in living cells at nM nocodazole concentrations. *BIOSENS. BIOELECTRON*, 16(9):773–782, 2001.

[2] C. Zhang, G. Feng, and Z. Gao. Development of a new kind of dual modulated QCM biosensor. *Biosens Bioelectron*, 12(12):1219–25, 1997.

[3] V. Glezer and O. Lev. Sol-gel vanadium pentaoxide glucose biosensor. *Journal of the American Chemical Society*, 115(6):2533–2534, 1993.

[4] R.D. Rauh. Metal oxide matrix biosensors, July 13 1999. US Patent 5,922,183.

[5] DT Hoa, T.N.S. Kumar, NS Punekar, RS Srinivasa, R. Lal, and AQ Contractor. A biosensor based on conducting polymers. *Analytical Chemistry*, 64(21):2645–2646, 1992.

[6] M. Gerard, A. Chaubey, and BD Malhotra. Application of conducting polymers to biosensors. *Biosens Bioelectron*, 17(5):345–59, 2002.

[7] L. Sabbatini L. Torsi, A. Dodabalapur and P. G. Zambonin. Multi-parameter gas sensors based on organic thin-film-transistors. *Sensors and Actuators B: Chemical*, 67(3):312–316, September 2000.

[8] L. Torsi, N. Cioffi, C. Di Franco, L. Sabbatini, PG Zambonin, and T. Bleve-Zacheo. Organic thin film transistors: from active materials to novel applications. *Solid State Electronics*, 45(8):1479–1485, 2001.

[9] B. Crone et al. Electronic sensing of vapors with organic transistors. *Applied Physics Letters*, 78(15):2229, 2001.

[10] Z.T. Zhu, J.T. Mason, R. Dieckmann, and G.G. Malliaras. Humidity sensors based on pentacene thin-film transistors. *Applied Physics Letters*, 81:4643, 2002.

[11] L. Wang. Nanoscale chemical sensor based on organic thin-film transistors. *Applied Physics Letters*, 85(26):6386, 2004.

[12] HE Katz, C. Huang, J. Huang, K. See, J. Miragliotta, and A. Becknell. Organic Field-effect Transistor Channel Perturbation at Two Surfaces through Analyte Binding and Dielectric Charging. *Semiconductor Device Research Symposium, 2005 International*, pages 228–229, 2005.

[13] LA Majewski, R. Schroeder, M. Voigt, and M. Grell. High performance organic transistors on cheap, commercial substrates. *Journal of Physics D, Applied Physics*, 38(24):3367–3372, 2004.

[14] Z. Bao. Materials and Fabrication Needs for Low-Cost Organic Transistor Circuits. *Advanced Materials*, 12(3):227–230, 2000.

[15] EJ Meijer, DM De Leeuw, S. Setayesh, E. Van Veenendaal, BH Huisman, PWM Blom, JC Hummelen, U. Scherf, and IM Klapwijk. Solution-processed ambipolar organic field-effect transistors and inverters. *Nature Materials*, 2(10):678–682, 2003.

[16] S.R. Forrest. The path to ubiquitous and low-cost organic electronic appliances on plastic. *Nature*, 428(6986):911–918, 2004.

[17] SR Forrest. Active optoelectronics using thin-film organic semiconductors. *Selected Topics in Quantum Electronics, IEEE Journal of*, 6(6):1072–1083, 2000.

[18] E. Huitema, G. Gelinck, B. van der Putten, E. Cantatore, E. van Veenendaal, L. Schrijnemakers, B.H. Huisman, D. de Leeuw, P. Res, and N. Eindhoven. Plastic transistors in active-matrix displays. *Solid-State Circuits Conference, 2003. Digest of Technical Papers. ISSCC. 2003 IEEE International*, pages 380–381, 2003.

[19] G. Horowitz. Organic Field-Effect Transistors. *Advanced Materials*, 10(5):365–377, 1998.

[20] F. Gutmann and L.E. Lyons. *Organic Semiconductors*. J. Wiley and sons, Inc., 1967.

[21] Terje A. Skotheim, editor. *Handbook of Conducting Polymers*, volume I, chapter 1, pages 1–43. CRC, 1986.

[22] G.G. Wallace, P.C. Dastoor, D.L. Officer, and C.O. Too. Conjugated polymers: New materials for photovoltaics. *Chem. Innov*, 30(1):14–22, 2000.

[23] H. Murata, GG Malliaras, M. Uchida, Y. Shen, and ZH Kafafi. Non-dispersive and air-stable electron transport in an amorphous organic semiconductor. *Chem. Phys. Lett*, 339:161, 2001.

[24] Qinghuang Lin, Raymond Pearson, and Jeffrey C. Hedrick, editors. *ACS Symposium Series 874: Polymers for Microelectronics and Nanolelectronics*, volume 874, chapter 1, pages 1–14. ACS Symposium Sries, 2004.

[25] J. Locklin and Z. Bao. Effect of morphology on organic thin film transistor sensors. *Analytical and Bioanalytical Chemistry*, 384(2):336–342, 2006.

[26] DJ Gundlach, YY Lin, TN Jackson, SF Nelson, and DG Schlom. Pentacene organic thin-film transistors-molecular ordering and mobility. *Electron Device Letters, IEEE*, 18(3):87–89, 1997.

[27] A. Di Carlo, F. Piacenza, A. Bolognesi, B. Stadlober, and H. Maresch. Influence of grain sizes on the mobility of organic thin-film transistors. *Applied Physics Letters*, 86:263501, 2005.

[28] B. Stadlober, V. Satzinger, H. Maresch, D. Somitsch, A. Haase, H. Pichler, W. Rom, and G. Jakopic. Structural and electrical properties of polymorphic pentacene thin films. *Proceedings of SPIE*, 5217:112–123, 2003.

[29] S. Pratontep, M. Brinkmann, F. Nüesch, and L. Zuppiroli. Correlated growth in ultrathin pentacene films on silicon oxide: Effect of deposition rate. *Physical Review B*, 69(16):165201, 2004.

[30] B. Servet, G. Horowitz, S. Ries, O. Lagorsse, P. Alnot, A. Yassar, F. Deloffre, P. Srivastava, R. Hajlaoui, et al. Polymorphism and Charge Transport in Vacuum-Evaporated Sexithiophene Films. *Chemistry of Materials*, 6(10):1809–1815, 1994.

[31] WA Schoonveld, RW Stok, JW Weijtmans, J. Vrijmoeth, J. Wildeman, and TM Klapwijk. Morphology of quaterthiophene thin films in organic field effect transistors. *Synthetic Metals*, 84(1):583–584, 1997.

[32] Y.Y. Lin, DI Gundlach, SF Nelson, and TN Jackson. Pentacene-based organic thin-film transistors. *Electron Devices, IEEE Transactions on*, 44(8):1325–1331, 1997.

[33] P. Stallinga et al. Electronic transport in field-effect transistors of sexithiophene. *Journal of Applied Physics*, 96(9):5277, 2004.

[34] G. Horowitz and ME Hajlaoui. Mobility in Polycrystalline Oligothiophene Field-Effect Transistors Dependent on Grain Size. *Advanced Materials*, 12(14):1046–1050, 2000.

[35] V.C. Sundar, J. Zaumseil, V. Podzorov, E. Menard, R.L. Willett, T. Someya, M.E. Gershenson, and J.A. Rogers. Elastomeric Transistor Stamps: Reversible Probing of Charge Transport in Organic Crystals, 2004.

[36] M. Mushrush, A. Facchetti, M. Lefenfeld, H.E. Katz, and T.J. Marks. Easily processable phenylene-thiophene-based organic field-effect transistors and solution-fabricated nonvolatile transistor memory elements. *J. Am. Chem. Soc*, 125(31):9414–9423, 2003.

[37] H.E. Katz, T. Siegrist, M. Lefenfeld, P. Gopalan, M. Mushrush, B. Ocko, O. Gang, and N. Jisrawl. Mesophase transitions, surface functionalization, and growth mechanism of semiconducting 6PTTP6 films from solution. *J. Phys. Chem. B*, 108(25):8567–8571, 2004.

[38] Karsten Krüger. Characterization of thiol-based semiconductor molecules and functionalization of silicon surfaces for dna attachment. Master's thesis, Rutgers University, 2006.

[39] F. Uslu, S. Ingebrandt, D. Mayer, and S. Böcker-Me. ert, M. Odenthal und A. O enhäusser. Labelfree fully electronic nucleic acid detection system based on a eld-e ect transistor device. *Biosensors and Bioelectronics*, 19:1723–1731, 2004.

[40] HE Katz, L. Torsi, and A. Dodabalapur. Synthesis, Material Properties, and Transistor Performance of Highly Pure Thiophene Oligomers. *Chemistry of Materials*, 7(12):2235–2237, 1995.

[41] L.H. Hall, C.R. Schraeder, and J.A. Sees. Piranha etch preparation having long shelf life and method of making same, September 25 2001. US Patent 6,294,145.

[42] G. Sauerbrey. The use of quartz oscillators for weighing thin layers and for microweighing. *Z Phys*, 155:206–222, 1959.

[43] V.M. Mecea. From Quartz Crystal Microbalance to Fundamental Principles of Mass Measurements. *Analytical Letters*, 38(5):753–767, 2005.

[44] A. Wajid. On the accuracy of the quartz-crystal microbalance (QCM) in thin-film depositions. *Sensors and Actuators A: Physical*, 63(1):41–46, 1997.

[45] HE Katz. Organic molecular solids as thin film transistor semiconductors. *J. Mater. Chem*, 7:369–376, 1997.

[46] Gary E. McGuire, editor. *Semiconductor materials and process technology handbook*, chapter The Thermal Oxidation of Silicon and Other Semiconductor Materials, pages 46–79. Noyes Publications, Park Ridge, NJ, 1988.

[47] C.D. Dimitrakopoulos and D.J. Mascaro. Organic thin-film transistors: A review of recent advances. *IBM Journal of Research and Development*, 45(1):11–28, 2001.

[48] R. Schroeder, L. A. Majewski, and M. Grell. A study of the threshold voltage in pentacene organic field-effect transistors. *Applied Physics Letters*, 83(15):3201–3203, 2003.

[49] G. Horowitz, R. Hajlaoui, H. Bouchriha, R. Bourguiga, and M. Hajlaoui. The concept of threshold voltage in organic field-effect transistors. *Adv. Mater*, 10:923–927, 1998.

[50] Gilles Horowitz, Xuezhou Peng, Denis Fichou, and Francis Garnier. The oligothiophene-based field-effect transistor: How it works and how to improve it. *Journal of Applied Physics*, 67(1):528–532, 1990.

[51] K. Seshadri and C.D. Frisbie. Potentiometry of an operating organic semiconductor field-effect transistor. *Applied Physics Letters*, 78:993, 2001.

[52] H. Klauk, G. Schmid, W. Radlik, W. Weber, L. Zhou, C.D. Sheraw, J.A. Nichols, and T.N. Jackson. Contact resistance in organic thin film transistors. *Solid State Electronics*, 47(2):297–301, 2003.

[53] R. Schroeder. Improving organic transistor performance with Schottky contacts. *Applied Physics Letters*, 84(6):1004, 2004.

[54] Josephine Bea Chang. *Functionalized Polythiophene Thin-Film Transistors for Low-Cost Gas Sensor Arrays*. PhD thesis, EECS Department, University of California, Berkeley, April 24 2006.

[55] G. Binnig, C. F. Quate, and Ch. Gerber. Atomic force microscope. *Phys. Rev. Lett.*, 56(9):930–933, Mar 1986.

[56] Paul E. West. *Introduction to Atomic Force Microscopy: Theory, Practice, Applications*. Pacific Nanotech, 2003.

[57] Paul E. West and Arthur Ross. *Introduction to Atomic Force Microscopy Modes*. Pacific Nanotech, 2006.

[58] V. Singh, M. Yano, W. Takashima, and K. Kaneto. Study of Gate Induced Channel in Organic Field Effect Transistors Using Poly (3-hexylthiophene) Films. *Japanese Journal of Applied Physics*, 45(1B):534–537, 2006.

[59] F.J. Giessibl. Advances in atomic force microscopy. *Reviews of Modern Physics*, 75(3):949–983, 2003.

[60] S. Pratontep, F. Nüesch, L. Zuppiroli, and M. Brinkmann. Comparison between nucleation of pentacene monolayer islands on polymeric and inorganic substrates. *Physical Review B*, 72(8):85211, 2005.

[61] G. Horowitz. Gate voltage dependent mobility of oligothiophene field-effect transistors. *Journal of Applied Physics*, 85(6):3202, 1999.

[62] R. Capelli, F. Dinelli, MA Loi, M. Murgia, R. Zamboni, and M. Muccini. Ambipolar organic light-emitting transistors employing heterojunctions of n-type and p-type materials as the active layer. *J. Phys.: Condens. Matter*, 18:S2127–S2138, 2006.

[63] D.M. DeLongchamp, S. Sambasivan, D.A. Fischer, E.K. Lin, P. Chang, A.R. Murphy, J.M.J. FrØchet, and V. Subramanian. Direct Correlation of Organic Semiconductor Film Structure to Field-Effect Mobility*. *J. Am. Chem. Soc*, 126:5207, 2004.

[64] D. Knipp, R. A. Street, A. Volkel, and J. Ho. Pentacene thin film transistors on inorganic dielectrics: Morphology, structural properties, and electronic transport. *Journal of Applied Physics*, 93(1):347–355, 2003.

[65] C.D. Sheraw, T.N. Jackson, D.L. Eaton, and J.E. Anthony. Functionalized Pentacene Active Layer Organic Thin-Film Transistors. *Advanced Materials*, 15(23):2009–2011, 2003.